

**AD-A253 348**



**RL-TR-92-2**  
**Final Technical Report**  
**February 1992**

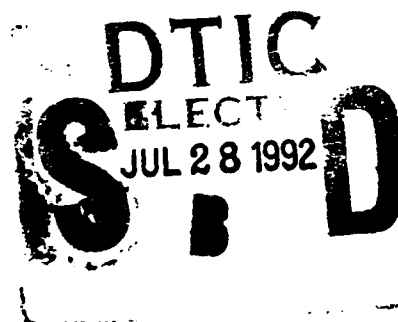


2

# **LONG WAVELENGTH MULTIPLE QUANTUM WELL LASERS FOR HIGH-SPEED MODULATION APPLICATIONS**

**PCO, Inc.**

**R.M. Ash, D.J. Robbins, A.K. Wood**



*This information contained herein is the property of GEC-Marconi Limited and is supplied without liability for errors or omissions. This material may be reproduced by or for the U.S. Government pursuant to the copyright license under the clause at DFARS 252.227-7013 (Oct 1988).*

**APPROVED FOR PUBLIC RELEASE; DISTRIBUTION UNLIMITED**

**92-20198**



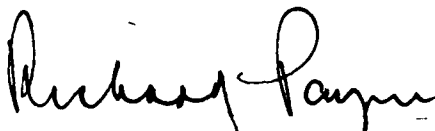
**92 7 27 115**

**Rome Laboratory**  
**Air Force Systems Command**  
**Griffiss Air Force Base, NY 13441-5700**

This report has been reviewed by the Rome Laboratory Public Affairs Office (PA) and is releasable to the National Technical Information Service (NTIS). At NTIS it will be releasable to the general public, including foreign nations.

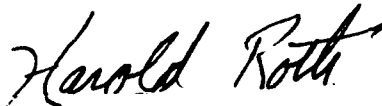
RL-TR-92-2 has been reviewed and is approved for publication.

APPROVED:



RICHARD PAYNE, Chief  
Electro-Optical Device Tech Division

FOR THE COMMANDER:



HAROLD ROTH, Director  
Solid State Sciences Directorate

If your address has changed or if you wish to be removed from the Rome Laboratory mailing list, or if the addressee is no longer employed by your organization, please notify RL( ERO ) Hanscom AFB MA 01731-5000. This will assist us in maintaining a current mailing list.

Do not return copies of this report unless contractual obligations or notices on a specific document require that it be returned.

# REPORT DOCUMENTATION PAGE

Form Approved  
OMB No. 0704-0188

Public reporting burden for this collection of information is estimated to average 1 hour per response, including the time for reviewing instructions, searching existing data sources, gathering and maintaining the data needed, and completing and reviewing the collection of information. Send comments regarding this burden estimate or any other aspect of this collection of information, including suggestions for reducing this burden, to Washington Headquarters Services, Directorate for Information Operations and Reports, 1215 Jefferson Davis Highway, Suite 1204, Arlington, VA 22202-4302, and to the Office of Management and Budget, Paperwork Reduction Project (0704-0188), Washington, DC 20503.

1. AGENCY USE ONLY (Leave Blank)		2. REPORT DATE February 1992		3. REPORT TYPE AND DATES COVERED Final	
4. TITLE AND SUBTITLE LONG WAVELENGTH MULTIPLE QUANTUM WELL LASERS FOR HIGH-SPEED MODULATION APPLICATIONS				5. FUNDING NUMBERS C - F19628-89-C-0136 PE - 61102F PR - 4600 TA - 19 WU - 69	
6. AUTHOR(S) R. M. Ash, D. J. Robbins, A. K. Wood					
7. PERFORMING ORGANIZATION NAME(S) AND ADDRESS(ES) PCO, Inc. 20200 Sunburst Street Chatsworth CA 91311-6289				8. PERFORMING ORGANIZATION REPORT NUMBER	
9. SPONSORING/MONITORING AGENCY NAME(S) AND ADDRESS(ES) Rome Laboratory (ERO) Hanscom AFB MA 01731-5000				10. SPONSORING/MONITORING AGENCY REPORT NUMBER RL-TR-92-2	
11. SUPPLEMENTARY NOTES Rome Laboratory Project Engineer: Andrew Davis/ERO(617)377-3598					
12a. DISTRIBUTION/AVAILABILITY STATEMENT Approved for public release; distribution unlimited.				12b. DISTRIBUTION CODE	
13. ABSTRACT (Maximum 200 words)  The goal of this work is the fabrication of quantum well lasers capable of being modulated at high speeds. The intrinsic laser resonance response and parasitic electrical effects combine to limit laser speed. The high gain-slope of multiple quantum well structures was used to overcome the first problem, that is, the fabricated lasers had InGaAsP/InP active regions. Low-pressure MOVPE was used to fabricate the devices. The goal was to design a laser that emits at 1.3 microns, which is the optional wavelength for fiber-optic communications. The first devices fabricated had high threshold current and low efficiency, but they confirmed the accuracy of the chosen model. An eight quantum well structure was chosen to minimize the deleterious effects of damping on the laser's frequency response. The final deliverable product had a threshold current of 10mA and an output power of 20mW. It operated out to 8 GHz and up to 100°C. It is believed diffusion capacitance from the leakage current limits frequency response.					
14. SUBJECT TERMS Lasers, quantum wells, MOVPE				15. NUMBER OF PAGES 64	
				16. PRICE CODE	
17. SECURITY CLASSIFICATION OF REPORT UNCLASSIFIED	18. SECURITY CLASSIFICATION OF THIS PAGE UNCLASSIFIED	19. SECURITY CLASSIFICATION OF ABSTRACT UNCLASSIFIED	20. LIMITATION OF ABSTRACT U/L		

# Contents

## 1. Summary

## 2. Technical report

### 2.1 Introduction

### 2.2 Theory and design

### 2.3 Growth

2.3.1 Materials Growth and Assessment

2.3.2 Growth of GaAlInAs Laser Wafers

2.3.3 Growth of Bulk GaInAsP Test Layers

2.3.4 Growth of MQW Test Structures

2.3.5 Growth of MQW Laser Diode Structures

### 2.4 Processing

2.4.1 Broad area oxide stripe lasers.

2.4.2 Buried ridge lasers.

2.4.3 The fabrication of buried ridge lasers on semi-insulating substrates.

2.4.4 Identification of processed wafers

### 2.5 Testing

2.5.1 Test methods

2.5.2 Measurement results

2.5.3 Conclusions

### 2.6 RF Testing

2.6.1 Test fixture and test methods.

2.6.2 Measurement technique.

2.6.3 Measurement results.

## 3. Conclusions

## 4. Deliverables

## 5. Suggestions for future work

## 6. References

## 7. Figures

ALL INFORMATION CONTAINED HEREIN IS UNCLASSIFIED

<b>Accession For</b>	
NTIS GRA&I	<input checked="checked" type="checkbox"/>
DTIC TAB	<input type="checkbox"/>
Unannounced	<input type="checkbox"/>
Justification	
By _____	
Distribution/	
Availability Codes	
Dist	Avail and/or Special
A-1	

Use, duplication or disclosure of data contained on this sheet is subject to the restrictions on the title page of this document.

## 1. Summary

The work reported here is aimed at exploiting some of the properties of quantum wells for the fabrication of semiconductor lasers which are capable of being modulated at high speed. In lasers the speed of operation is limited by the intrinsic resonance response of the laser (which arises from the non-linear interaction between the optical field and electrical carriers within the structure) and by parasitic electrical effects such as capacitance, resistance and inductance of the laser chip and of the packaging.

The programme of work reported here addressed the first of these factors by investigating the use of multiple quantum wells (MQWs) to form the active region of the laser. MQW devices have many interesting properties, but the main one to be exploited for this application is the higher gain-slope which, like most MQW properties, results from the changes in the band structure with reduced dimensionality. The chip and packaging parasitics were not explicitly addressed within this programme since GEC-Marconi already had significant experience in the fabrication of low capacitance laser structures.

The main body of the work was to design structures for emission at  $1.3\mu\text{m}$  using existing models, to grow and characterize a series of calibration and test wafers using low pressure metallo-organic vapour phase deposition (MOVPE) and to fabricate these into test devices. Two representative devices bonded into test fixtures suitable for testing in the laboratory are supplied as deliverables.

During the programme 36 wafers were grown, together with additional secondary growths to fabricate complete laser structures. Six wafers were processed into lasers of various types, including three into low capacitance structures for high speed. All the lasers were tested for basic performance characteristics, and the low capacitance devices were measured at high speed. Operation up to 10GHz was achieved, with, it is believed, performance beyond this being limited by leakage currents in the laser structure.

## 2. Technical Report

### 2.1 Introduction

Early work on quantum well lasers for  $1.3\mu\text{m}$  operation was almost exclusively based upon LPE, and although very encouraging results were reported in this area by a number of groups [1-3], the structures that could be obtained were limited by the growth technique to relatively thick wells and barriers. Nevertheless, this work allowed some of the potential advantages of quantum well structures for  $1.3\mu\text{m}$  emitters to be demonstrated; reduced threshold current densities ( $410\text{A}/\text{cm}^2$  for  $2.2\text{mm}$  long devices [3]); reduced linewidth enhancement factor  $\sim 2$  [2], and increased resonant frequency ( $9\text{GHz}$  at  $5.3\text{mW}/\text{facet}$  [2]), and this was the position at the start of this programme. Our own work [4] on an InGaAlAs based (graded-index separate confinement heterostructure) GRIN-SCH quantum well laser at  $1.3\mu\text{m}$  was among the first of a small number of papers to emerge during the last two to three years exploiting first LP-MOCVD [5-10], and latterly, GSMBE [11]. Initially [5,6] these devices were simple multiple quantum well (MQW) designs based on  $200\text{\AA}$  wide,  $1.34\mu\text{m}$ -InGaAsP quaternary wells, and InP barriers, which exhibited  $T_0 \sim 57\text{K}$ ,  $I_{th} \sim 35\text{mA}$  and  $\eta_D \sim 45\%$ . More recent developments have included the addition of a simple outer guide region [11] which parallels our own work, a 'stepped' quasi-GRIN outer confinement region [7-9], and a full GRIN structure [10]. Threshold currents of  $15\text{mA}$  have been obtained on  $400\mu\text{m}$  buried heterostructure devices with threshold current densities of  $540\text{A}/\text{cm}^2$  on  $1\text{mm}$  long broad area structures [11]. CW output powers up to  $100\text{mW}$  have also been reported [8].

### 2.2 Theory and Design

The computer model used in the theory and design work on this programme was described in the final report for research contract F19628-85-C-0172 [12]. In [12] it was concluded that quantum well laser designs with an outer confinement region, i.e. 'modified' or 'GRIN' structures, were essential if low threshold long wavelength lasers were to be successfully developed. Clearly, either of the quaternary materials systems, InGaAsP or GaAlInAs lattice matched to InP, could be used in more sophisticated structures, and it appeared initially that the tri-metal quaternary InGaAlAs was the preferred route to achieving this end. There were two clear reasons for this, primarily the ability to exchange Al for Ga in this material (rather as in

GaAlAs) brings GRIN structures more easily within reach, secondly, the heterojunction offset lies mainly in the conduction band making it easier to achieve good carrier confinement and to uniformly pump the wells. The refractive index difference is also larger in InGaAlAs/InP than for comparable structures in InGaAsP/InP which is an additional small bonus while the staggered heterojunction lineup between the tri-metal quaternary and InP is not a problem, provided that this heterojunction lies within the heavily doped contact regions of the device. There are, however, difficulties associated with the MOCVD growth of AlGaInAs, particularly with regard to oxygen incorporation, and regrowth in multistage epitaxy, which lead us to move to the InGaAsP/InP system in this programme. Perhaps less widely appreciated, the thermal conductivity of the Al containing compounds is also relatively poor. Excellent results for 1.55 $\mu$ m quantum well lasers have been published in both materials systems, however, and the balance of advantages between the two materials systems has been rather well reviewed recently by Greene et. al. [13].

The software tools described in [12] have been applied to the design of 1.3 $\mu$ m quantum well lasers in InGaAsP/InP. The object of the initial design work was to produce a relatively 'safe' device specification centered around the requirement for low threshold current. Since the difficulties inherent in grading the InGaAsP quaternary precluded the use of GRIN structures at that time the simpler multiple quantum well structure modified by an outer confining well was adopted. The choice of quaternary composition for the outer well is, however, more severely constrained for 1.3 $\mu$ m operation than at 1.55 $\mu$ m, by the conduction band offsets available. Assuming that  $\Delta E_c/\Delta E_g \sim 0.4$  (see for example [14]), these are plotted in figure 1 as a function of the bandgap wavelength of the outer quaternary. In a series of papers, Nagle and Weisbuch [15-16] have shown clearly that an inner confinement ( $\Delta E_{c2}$ ) of at least 2kT is required to avoid very significant loss due to spontaneous emission from the outer well, and in the current work  $\lambda_g = 1.07\mu$ m quaternary barriers were specified providing  $\sim 3kT$  for both inner and outer electron confinement.

Having established the composition of the outer well other details of the design fall rapidly into place. The emission wavelength can be controlled by both well width and well alloy composition. As shown in [12] emission at 1.3 $\mu$ m could be obtained using InGaAs wells  $\sim 30$ -40 $\text{\AA}$  in width, and in [10] a four 50 $\text{\AA}$ ,  $\lambda_g = 1.39\mu$ m, quaternary well active layer structure is described. However, the large band-edge density-of-states in such narrow wells leads to high carrier densities which are not desirable. Rather, the approach taken here was to work with relatively wide wells, 100 $\text{\AA}$ , of 1.3 $\mu$ m quaternary, which retains essentially single sub-band

pair operation. Optical confinement factors are plotted in figure 2 showing the dependence upon outer well width ( $d$  defined in the inset of figure 2), and in figure 3 as a function of well number for  $d=1000\text{\AA}$ , assuming an active region composed of  $100\text{\AA}$  wells of  $1.3\mu\text{m}$  quaternary. Simulations of the threshold characteristics were performed assuming an energy dependent Lorentzian broadening of  $10\text{meV}$  FWHM at the band edge, decaying linearly to a  $2\text{meV}$  background value at  $65\text{meV}$  above the sub-band edge. In this respect the model differs from that described in [12]; for a fuller discussion see [17]. Strictly the broadening will depend weakly upon carrier density but in order to reduce the computational burden this second order effect was neglected. An Auger recombination coefficient of  $2.5 \cdot 10^{-29} \text{ cm}^6\text{s}^{-1}$  [18-20] and an intervalence band absorption coefficient of  $15\text{cm}^{-1}$  at a carrier density of  $10^{18} \text{ cm}^{-3}$  [21] were assumed. These values are typical of bulk lasers but there is now a significant body of literature to support the view that this is a sufficient approximation for quantum wells.

In a series of figures, threshold characteristics parametrised by the total loss (cavity and mirror loss) are given: spontaneous emission current density (figure 4); total current density (figure 5); lasing emission energy (figure 6), and gainslope (figure 7). For small numbers of active wells the current densities are seen to rise rapidly (figure 5) with an associated jump in lasing wavelength away from  $1.3\mu\text{m}$  to the higher order transition. It was concluded that structures with five active wells would be most suitable for the initial design. Figure 6 shows that the predicted emission wavelength is within  $\sim 5\text{meV}$  of the required  $1.3\mu\text{m}$  emission wavelength. The calculation of this wavelength depends upon a combination of band-gap narrowing and band filling and so is subject to some error. In subsequent iterations of the device design a small adjustment of the quaternary composition of the active layers may be necessary to achieve a given emission wavelength. Finally the Fermi energy levels for typical threshold carrier densities are plotted in figure 8. Spontaneous emission in the outer confinement layer has not been included in these calculations, but figure 8 shows that the electron Fermi-energy will in fact be above the band-edge of the cladding quaternary in most cases (for the five well structure the threshold carrier density is expected to be  $\sim 1.9 \cdot 10^{18} \text{ cm}^{-3}$ , for  $\alpha = 25\text{cm}^{-1}$ ), so that this could still form a significant contribution to the total current, particularly for smaller numbers of wells in the active region.

The final device specification, although arrived at independently (see figure 27 for a schematic), is similar to others in the literature [7-11] where 3,4 and 5 well structures have been investigated.



The frequency response of the laser can be written as the product of, the intrinsic device response ( $R_{\text{Device}}(f)$ ), and the external 'circuit plus parasitic' response  $R_{\text{RC}}(f)$ , so that,

$$R(f) = R_{\text{Device}}(f) \cdot R_{\text{RC}}(f) = \frac{1}{1 - \left(\frac{f}{f_{\text{res}}}\right)^2 + \frac{if\Gamma}{2\pi f_{\text{res}}^2}} \cdot \frac{1}{1 + \left(\frac{f}{f_{\text{RC}}}\right)^2}$$

where  $f_{\text{res}}$  is the resonance frequency,  $\Gamma$  is the damping factor and  $f_{\text{RC}}$  the roll off frequency of the extrinsic elements. Simple equivalent circuit models show that in order to effectively remove the influence of  $R_{\text{RC}}(f)$  up to  $\sim 15\text{GHz}$ , the parasitic (bondwire) inductances should be  $\leq 0.5\text{ pH}$ , (contact plus access) resistance  $\leq 3\text{ Ohms}$  and the device capacitance  $\leq 2\text{ pF}$ . The resonance frequency, which depends upon current, is proportional to the square root of the gainslope and so, naively, a larger gainslope implies better rf performance, and figure 7 shows that the calculated gainslope for these quantum well devices is a factor of  $\sim 5$  larger than that typical of bulk  $1.3\mu\text{m}$  DH lasers. It has become clear during the course of this programme that this simple argument is inadequate because the damping factor is also larger in quantum well lasers, and only in strained layer quantum well devices does a significant advance in speed now appear possible. The possible mechanisms behind this are the subject of current debate, and a full discussion lies beyond the scope of this report, however, it appears that there is a dependence of quantum well laser speed on the structure of the guide and active regions which favours an increase in the number of wells in the active layer and hence a reduced carrier density. The increased damping leads to the conclusion that an 8 well structure might give a better high frequency performance than a 5 well structure owing to the reduction in damping. The last wafer grown, OF912, had 8 wells with this in mind.

## 2.3 Growth

### 2.3.1 Materials Growth and Assessment.

All the material grown, as described below, was achieved using a CVT MOCVD 4000 growth reactor. The reactor consists of a horizontal quartz reactor tube supporting a graphite susceptor, housed in a circular section low pressure vessel. The reactor operates at 150 Torr. The reactor is heated using an inductively coupled RF heating system enabling the temperature to be accurately controlled to within  $1^\circ\text{C}$ . The critical features of the reactor with respect to the

growth of MQW structures are the use of a radial geometry fast switching manifold to allow the fast exchange of reagent gases entering the reactor, and the use of multiple sources allowing quaternaries of different compositions to be set up and switched into the reactor using the fast switching manifold when they are required, eliminating the need for growth pauses to allow for settling. All growths were carried out using alkyl Gp. III precursors (tri-methyl indium, tri-methyl gallium, tri-ethyl gallium and tri-ethyl aluminium) and hydride Gp. V precursors ( $\text{AsH}_3$  and  $\text{PH}_3$ ).  $\text{H}_2\text{S}$  (2000 vpm in hydrogen balance) and di-methyl zinc (500 vpm in hydrogen balance) were used as n and p type dopants respectively.

The growth of complex device structures such as MQW lasers requires that as much characterisation information as possible is obtained first regarding the constituent parts of the laser structure individually, before growth of the full structure takes place. The need for quaternary quantum wells for efficient device operation at  $1.3\mu\text{m}$ , as discussed in section 2.1 requires a significant amount of materials growth development compared with the  $1.55\mu\text{m}$  devices that are fabricated for the telecommunications market. Hence, the growth of the MQW lasers took place in three stages :

- i) Growth and characterisation of bulk layers of the quaternary materials required for the laser structure. This involves an iterative process towards obtaining the required alloy composition by using an empirically derived function relating easily measured parameters of the epitaxial layers to the alloy composition.
- ii) Growth and assessment of MQW test layers involving up to 90 periods of well and barrier. This allows the assessment of the MQW material for interface perfection and luminescence wavelength.
- iii) Growth and assessment of full laser diode structures.

Using this three stage process it is possible to individually characterise each part of the structure before the growth of a complete structure.

In total, to achieve this, thirty six growths were carried out comprising :

- 2 GRIN-SCH GaAlInAs laser device wafers
- 17 Quaternary composition calibration growths.
- 9 Multiple quantum well test structure growths.
- 6 Full laser device growths.
- 2 Aborted growths.

Table 1. Growth Summary

The key features of these growths are summarised in the following sections

### 2.3.2 Growth of GaAlInAs laser wafers.

At the start of the programme the GaAlInAs materials system was proposed as the growth vehicle for the fabrication of MQW lasers. This materials system has considerable advantages as discussed in section 2.1. Two wafers were grown to a specification aimed at this requirement. No calibration runs were required for this work since devices had already been made in this system prior to the start of the programme [4]. The layer structure grown is shown in figure 9.

The wafers were characterized using X-ray diffractometry, photoluminescence spectroscopy and TEM. The uniformity of photoluminescence is shown in the map of figure 10. Assessment data for these wafers is summarized in Table 2.

Parameter	OE1075	OE1077
Photoluminescence peak $\lambda$ (nm)	1277	1281
Photoluminescence $\sigma$ (nm)	3.8	13.5
TEM wells ( $\text{\AA}$ )	75	70
TEM barriers ( $\text{\AA}$ )	103	93
TEM grades ( $\text{\AA}$ )	1037	1066

Table 2 Assessment data for wafers OE1075 and OE1077

The performance of finished devices made from this material are discussed in section 2.4. The lack of improvement in threshold current over prior attempts led us to concentrate on GaInAsP materials, which form the basis of the work discussed below. This materials system, whilst being more complex to control lattice match and offering a less favourable conduction band offset than GaAlInAs has the advantage of no aluminium, noted for its tendency to oxidise readily.

### 2.3.3 Growth of Bulk GaInAsP Test Layers.

Test layers of GaInAsP ( $\lambda_g=1.07\mu\text{m}$ ) and GaInAsP ( $\lambda_g=1.3\mu\text{m}$ ) were grown and assessed using double crystal X-ray diffractometry to assess the crystallographic quality and properties of the materials, and by photoluminescence (PL) spectroscopy to assess both the structural quality and the optical properties of the materials.

In order to achieve the required alloy composition it is necessary to calibrate the gas phase conditions with respect to the solid phase alloy compositions achieved. This involves an iterative process of growth, assessment to calculate the achieved alloy composition, calculation of a new set of gas phase conditions, and further growth. The calculation of a new set of gas phase conditions is done on the basis of an empirical data set collected over many growths, and relates the lattice constant (measured using double crystal X-ray diffractometry) and the energy bandgap (measured using PL) to the alloy composition, and suggests a set of gas phase conditions which will achieve a closer solid phase alloy composition to that required. For alloy compositions of materials not grown previously this iterative process can take many growths to achieve the final desired alloy composition, and indeed this was the case with the growth of the GaInAsP ( $\lambda_g = 1.07\mu\text{m}$ ) material. An additional problem is encountered with the growth of short wavelength quaternary materials in that the gas phase to alloy composition relationship is non-linear for the group V sub-lattice. Therefore, linear extrapolations of alloy composition for the group V sub-lattice will result in an incorrect resultant solid phase alloy composition. This problem is exacerbated because the gradient of the gas phase to solid phase alloy composition relation is high for these materials. Thus a small change in the gas phase concentrations of the reagents can lead to very large changes in the resultant solid phase alloy composition. Therefore, as can be seen from Table 1, which summarises the growths carried out for the fabrication of the full laser diode structures, half of the growths are calibration of the solid phase alloy compositions required for the MQW laser structures.

Figures 11 and 12 show a double crystal X-ray diffractogram and a PL spectrum respectively for a single layer of GaInAsP ( $\lambda_g = 1.07\mu\text{m}$ ). The structural quality of this epitaxial layer is attested to by the narrow linewidth (24 arcsecs) of the X-ray diffraction peak pertaining to the epitaxial layer and by the narrow spectral linewidth of the PL emission (41meV). In addition the separation of the peaks on the double crystal X-ray diffractogram shows that the epitaxial layer is lattice matched to the substrate to within 289 ppm.

Figures 13 and 14 show a double crystal X-ray diffractogram and a PL spectrum respectively for a single layer of GaInAsP ( $\lambda_g = 1.3\mu\text{m}$ ). As with the GaInAsP ( $\lambda_g = 1.07\mu\text{m}$ ) material the narrow linewidth of the diffraction peak pertaining to the epitaxial layer (30 arcsecs) and the narrow spectral linewidth of the PL emission (53meV) indicate high quality of the grown material. In addition the separation of the peaks on the X-ray diffractogram shows that the epitaxial layer is lattice matched to the substrate to within 467 ppm.

Having obtained the required solid phase alloy compositions it was then necessary to grow and assess MQW test structures.

#### 2.3.4 Growth of MQW Test Structures.

Test structures consisting of GaInAsP( $\lambda_g = 1.3\mu\text{m}$ )/GaInAsP( $\lambda_g = 1.07\mu\text{m}$ ) MQW structures of up to 90 periods of well and barrier have been grown and assessed using double crystal X-ray diffractometry, PL spectroscopy, transmission electron microscopy (TEM) and absorbance spectroscopy. The motivation for growing these types of test structures and assessing them using a wide range of analytical techniques is to measure and calculate the basic properties of the structure (well and barrier width and MQW period) and also to assess the structural and optical properties of the structures with regard to interfacial perfection and crystallographic quality of the layers which constitute the MQW period.

Initial growths of MQW test layers comprised 30 and 90 repeats of GaInAsP ( $\lambda_g = 1.3\mu\text{m}$ )/GaInAsP ( $\lambda_g = 1.07\mu\text{m}$ ) of thicknesses approximately 100Å each layer. Using this type of structure it is possible with double crystal X-ray diffractometry to measure the period of the MQW. A diffractogram from an MQW structure such as that shown in figure 15 is seen to consist of main diffraction peaks associated with the unit cell of the epitaxial layers and substrate lattices, and subsidiary maxima or satellites associated with the unit cell of MQW

super-lattice. The intensity of these satellites only becomes appreciable when the number of repeats in the MQW structure (and therefore the number of unit cells in the super-lattice) is sufficient to give a diffraction peak intensity greater than the X-ray background. Since GaInAsP ( $\lambda_g = 1.3\mu\text{m}$ ) and GaInAsP ( $\lambda_g = 1.07\mu\text{m}$ ) are very similar in their properties with regard to X-rays the number of repeats required is large ( $>30$ ). The spacing of the satellite peaks in reciprocal lattice space gives directly the period of the MQW structure. By making two growths, varying only the growth time for one of the constituent layers from one growth to the next, the growth rates for both the well and barrier within the MQW period can be calculated. (This assumes the growth rates for the well and barrier materials are constant regardless of layer thickness.) Information regarding the structural integrity of the constituent layers of the MQW period can be obtained from the X-ray diffractogram. As can be seen from figure 15, which shows a diffractogram from a 90 period MQW structure, the main peak has a narrow line width comparable to that of the peak corresponding to the substrate X-ray reflection, indicating the high quality of the quaternary GaInAsP layers.

Additional structural information can be obtained regarding the interfacial quality of the MQW structure using transmission electron microscopy (TEM) and absorbance spectroscopy. Figure 16 shows a TEM cross section view of a 15 well/14 barrier MQW structure. The dark bands on the TEM micrograph are the quantum wells and the lighter bands are the barriers. Surrounding the MQW structure are confinement layers of GaInAsP ( $\lambda_g = 1.07\mu\text{m}$ ). The mottling on the micrograph is due to thinning process required for TEM sample preparation. Although TEM will not show small variations in the well width and structure repeat in the plane of the growth, it will show ripples at the well/barrier hetero-interface due to interfacial strain and microscopic well and barrier width variations in the direction of growth. As can be seen from figure 16 no such variations (or interfacial rippling) are evident. Absorbance spectroscopy can give more information about the quality of the quantum well structure in terms of well width variations both in the plane of the epitaxial layers and in the growth direction. Figure 17 shows such an absorbance spectrum from a 30 period MQW structure. As can be seen from the spectrum the sample showed strong resonant features associated with the confined electronic states within the quantum well. Both  $c_1\text{-hh}_1$  and  $c_1\text{-lh}_1$  transitions are in evidence. Similar spectra from 5 well laser structure samples do not show such well defined resonance features. This is possibly due to the inclusion of dopants.

It was also necessary to calibrate the photoluminescent emission (PL) with respect to the well width. It was assumed the solid phase alloy composition of the quantum well material was the

same as that for the bulk quaternary layers described previously, so the peak PL emission wavelength was to be calibrated only on the basis of varying the quantum well width. An example of the room temperature PL emission is shown in figure 18. The spectrum shows a single peak commensurate with good quality quantum well material. In addition low temperature (10K) PL emission was assessed. The appearance of multiple peaks on a low temperature PL spectrum can indicate problems such as atomic ordering, with the spectral linewidth giving some indication of the quality of the MQW structure. Such a PL spectrum, is shown in figure 19. The spectrum shows a single peak of linewidth 11.5meV.

In summary, the use of double crystal X-ray diffractometry, TEM, absorbance spectroscopy and PL both at room temperature and low temperature (10K) has demonstrated that MQW layers of good quality and of the correct layer thicknesses can be grown. Having demonstrated this laser device layers were grown and assessed.

### 2.3.5 Growth of MQW Laser Diode Structures.

Four GaInAsP laser diode wafers, OF634, OF653, OF910, and OF912 were grown and assessed using some of the techniques described above. The result of assessment on these wafers is described below.

The first two device layers, OF634 and OF635 were grown to the specification shown in figure 20. OF634 was grown on an InP tin doped substrate, and consisted of a 5 well/4 barrier structure of 100Å well and barrier thickness surrounded by 1000Å of GaInAsP ( $\lambda_g=1.07\mu\text{m}$ ). The grown layer thickness data is summarised in Table 3

Layer	Thickness (Å)	
	Front Test Piece	Rear Test Piece
InP Guide	420	336
1.07Q Guide	1065	1028
Barriers	103	103
Wells	112	112
1.07Q Guide	1065	1028

Table 3 TEM thickness data for OF634

The peak PL emission wavelength was mapped over the full 2" wafer and the result of this is shown in figure 21, with each + indicating a measurement point. The variation in the PL wavelength follows a radial geometry indicating the wavelength uniformity is limited by wafer edge effects rather than thermal non-uniformities in the reactor or gas depletion effects. Figure 22 shows the corresponding 10K PL spectrum which has a single, narrow, 9.0meV wide peak, comparing favourably with measurements on earlier test structures.

The second device wafer, OF653, was grown on an iron doped InP substrate. It can be noted that the quantum well and barrier materials grown on this wafer are nearer to the required specification of thickness (measured by cleaved edge TEM) than for the previous wafer, OF634. The measurements are summarized in Table 4.

As with OF634 the peak PL emission wavelength was mapped over the full 2" wafer and the result of this is shown in figure 23. The wavelength follows an almost radially symmetric pattern, although there does appear to be some front to back variation in the wavelength. The reason for the difference in the character of the non-uniformity (compared with OF634) is not clear; however, it is known that the positioning of the wafer in the reactor is critical with regard to wavelength uniformity. In addition the low temperature (10K) PL shown in figure 24 shows a linewidth narrower (8.0meV) than that for the previous wafer and those for the test structures. Again it is not clear why this is, since the growth took the same form as with the growth of OF634 with some modification to the growth times for the growth of the well and barrier layers.

Layer	Thickness (Å)	
	Front Test Piece	Rear Test Piece
InP Guide	458	411
1.07Q Guide	981	953
Barriers	103	98
Wells	103	98
1.07Q Guide	1009	981

Table 4 TEM thickness data for OF653



OF910 was also grown to the specification shown in figure 20 on an iron doped InP substrate. There was no grown layer thickness information taken for this wafer since the PL peak emission wavelength was taken to be the more critical parameter than the actual quantum well thicknesses. A full 2" wafer peak wavelength map was taken for this sample and is shown in figure 25. Again the characteristic nature of the non-uniformity in wavelength is that of a radial geometry. It should also be noted that the measurement point density of this wavelength map is greater than that for the previous two wafers described. The effect of this will be to degrade the standard deviation in wavelength 'figure of merit' for this wafer with respect to the previous two wafers. However, the map does show an 11nm standard deviation from a mean of 1288nm. Low temperature PL spectrum from this wafer is shown in figure 26. As can be seen from this spectrum, there is a subsidiary peak at approximately 25meV lower energy than the main peak. The origin of this second peak is unknown.

OF912 was grown to the specification shown in figure 27 on an iron doped InP substrate. This consisted of 8 quantum wells and 7 barriers of thicknesses 100Å and 150Å respectively. The associated confinement layers were 750Å thick. As with the previous described wafer OF910 there were no thickness measurements taken for the same reasons as before.

A full 2" wafer peak wavelength map for this sample is shown in figure 28, with a standard deviation of 9.8nm at 1268nm. The typical radial characteristic of the PL wavelength is again seen. A low temperature PL spectrum from this wafer is shown in figure 29, which also shows a subsidiary peak at approximately 25meV lower energy than the main peak.

## 24 Processing

Three process routes have been used to evaluate the multiple quantum well material grown during the course of this programme:

- 1 The fabrication of broad area ("oxide stripe") lasers for the evaluation of basic materials quality.
- 2 The fabrication of buried ridge lasers for the evaluation of performance in an optically confined, small active volume structure.
- 3 The fabrication of buried ridge lasers on semi-insulating substrates, enabling low parasitic capacitance for high speed operation to be achieved.

The above structures have all been fabricated previously by GEC-Marconi. Their implementation with the  $\lambda_g=1.3\mu\text{m}$  MQW material described in section 2.2 forms the basis of this work. Brief details of the structures are described below to complete the technical description. Table 5 shows which wafers were processed through each process route.

#### 2.4.1 Broad area oxide stripe lasers.

These devices were fabricated using MQW source wafers grown on conducting (n-type) substrates early on in the program in order to establish the basic material quality. The layer structure for these wafers is shown in figure 30. The MQW part of the wafer was grown first, then in a subsequent growth operation, an InP guide layer and GaInAs contacting layer was added. The advantage of this two stage growth procedure is that the first growth has the same specification as that required for subsequent buried ridge laser fabrication, allowing validated material to be used for this process.

The fabrication continued with the deposition of a  $2000\text{\AA}$  thick silica layer, which was then patterned with photoresist, allowing etching of  $100\mu\text{m}$  wide windows in the oxide. The wafer was then metallized using TiZnAu, a metal combination having good ohmic contacting properties to GaInAs. After thinning the wafer and applying a contact to the back of the wafer (InGeAu), the wafer was cleaved up into individual chips of various lengths. A schematic of the final chips is shown in figure 31. These were then tested as described in section 2.5.

#### 2.4.2 Buried ridge lasers.

The fabrication of low threshold current and high speed lasers requires a structure with a small active volume. In order to prove the performance of the MQW material in a small active volume structure, before launching into a complex low capacitance design, buried ridge lasers were fabricated on MQW material grown to the same specification as in 2.3.1. The process sequence was to define narrow ridges in the MQW wafer by wet etching using a photoresist mask. The wafer was then overgrown with InP and GaInAs, as for the oxide stripe laser. The lower bandgap voltage of the MQW hetero-junction region compared with the InP homo-junction is such that current will flow preferentially through the active region in this structure. The wafer processing then continued with the addition of a proton implanted region all over the

wafer, with the exception of  $5\mu\text{m}$  each side of the active region, to reduce parasitic leakage currents. Detailed design of this type of laser structure is given in [22]. Silica was again deposited and etched, this time with a  $5\mu\text{m}$  wide window over the active region prior to metallization, thinning and back metallization. The addition of a window in the back metallization allowed viewing of the spontaneous emission through the transparent substrate. A gold plated heat spreader was added to the top of the wafer to improve thermal performance. A schematic of the finished chip is shown in figure 32. After cleaving into individual chips their performance was assessed as described in section 2.4.

#### 2.4.3 The fabrication of buried ridge lasers on semi-insulating substrates.

A very much more complex processing route was required to validate the high speed performance of the MQW material. The basic laser was of the buried ridge configuration as described above, but with the MQW layers grown on a semi-insulating (iron doped) InP substrate to allow low capacitance to be realized. Ridge etching and overgrowth with p-InP waveguide and p-GaInAs contacting layers were carried out conventionally. The sequence of processing is shown schematically in figures 33 (a) to (g). A  $5\mu\text{m}$  wide ohmic contact stripe of TiZnAu was deposited centrally over the active region, using a resist float-off technique. The wafer was then coated with  $\text{SiO}_2$  prior to sintering of the contact at  $425^\circ\text{C}$ . A channel was etched each side of the ridge using a photoresist mask to etch the oxide, then using the oxide as a mask to etch a channel (which also eliminates the need for a proton implantation step for current confinement). An InGeAu n-contact was floated off at the bottom of the etched channels, using the same resist mask as was used for the etch step. The whole surface was then covered with  $\text{SiO}_2$  prior to sintering the n-ohmic contact metal. An isolation channel was etched each side of the first channels down to the semi-insulating substrate using methane/hydrogen reactive ion etching (RIE). This provided electrical isolation of the regions outside these channels. The bond-pads on these areas, because they are electrically isolated from the remainder of the structure, contribute only a very small parasitic capacitance. The entire structure was planarized using polyimide and, after curing, via holes were etched in the polyimide using an  $\text{SiO}_2$  mask and oxygen RIE to access the n and p ohmic metals, and to provide a semiconductor rather than polyimide base for the wirebond pads outside the isolation channels. A second level metallization of  $1\mu\text{m}$  thick CrAu was sputtered onto the wafer. The metal was patterned to separate the n and p contact and bond-pad regions using an Ar/ $\text{Cl}_2$  ion beam milling system equipped with SIMS for endpoint detection [23]. The bond-pads

contribute only a very small amount to the capacitance because they are electrically isolated from the remainder of the structure by the isolation channels. Finally all exposed areas of polyimide were ashed off to allow cleaving of the lasers into individual die (250 $\mu$ m long). Figures 34 and 35 respectively show a schematic and an SEM micrograph of the finished laser chip.

#### 2.4.4 Identification of processed wafers

Table 5 indicates which wafers were selected for processing.

Wafer number	Oxide stripe lasers	Buried ridge lasers	Buried ridge lasers (SI substrate)
OE1077		X	
OF634	X	X	
OF653			X
OF910			X
OF912			X

Table 5      Wafers selected for processing

Testing of the devices for basic performance characteristics is described in section 2.5 and RF testing is described in section 2.6.

## 2.5      Testing

This section describes the CW and pulsed testing of the laser structures described above. The parameters were measured using established techniques and were aimed at assessing basic performance parameters such as threshold current density, wavelength of operation, thermal performance, power output properties, resistance and capacitance. For the tests described below the devices were measured after being soldered using lead/indium solder onto copper heatsinks and conventionally wirebonded using 25 $\mu$ m gold wire. The test methods used are

described below, followed by the measurement results in tabular form and then some conclusions.

### 2.5.1 Test methods

The operating wavelength of the devices was not a key parameter in the requirement, but was measured to assess the correlation between the emission wavelength and the wavelength measured using photoluminescence (PL) techniques (as described in section 2.3). It would be expected that there would be some difference between the techniques since PL uses very low excitation energies compared with operation under electrical pumping. Operating wavelength was measured using standard grating based monochromator apparatus with apertures small enough to resolve individual longitudinal modes in the devices.

Threshold current, output power and efficiency were measured under both pulsed and CW operation. By measuring in a pulsed mode, with pulses shorter than the thermal time constant of the chip and with low duty cycle, it is possible to investigate operation without heating the active region of the chip significantly. Pulses of 200ns length with a 10µs period were delivered via a 50Ω load to the chips. A computer controlled system allowed the pulses to be increased in amplitude to gradually ramp up the peak current in the laser chip. The output power and current during the pulse were measured with a linear gate system which allowed the computer to plot light-current transfer characteristics and to calculate external quantum efficiency from the slope of the light-current characteristic and a knowledge of the wavelength. CW measurements were made using the same system by inverting the output pulse. The threshold current density, the parameter used to characterize the basic gain/loss characteristics of the material in broad area oxide stripe lasers was measured in a similar way to the light current characteristics above.

The thermal performance of the lasers was measured by measuring light current characteristics as described above, with the package held at a range of temperatures with a thermoelectric cooler. The most useful data measured this way is the pulsed threshold current variation with temperature. The characteristic temperature of the laser,  $T_0$ , is given by  $\log_e(I_{th})/T$  where  $T$  is the temperature and  $I_{th}$  is the threshold current, which is found empirically to vary exponentially with temperature. At elevated temperatures; however, this relationship breaks down owing to the dominance of temperature dependent effects such as Auger and Inter-

Valence Band Absorption (IVBA). At modest temperatures, less than 50°C, a low  $T_0$  would indicate carrier leakage over the hetero-junction barriers in the structure, or poor confinement of the current to the active junction in a buried device.

Devices have also been characterized for electrical resistance and capacitance. Resistance measurements were carried out on bonded devices by simply measuring the voltage difference across the device for a given change in current above threshold. A four terminal measurement was used to ensure that the intrinsic device was measured rather than the resistance of the probe connections. Capacitance is not readily measured at the operating point, but was measured at zero bias and 1MHz by probing directly onto chips and using a commercial LCR meter. This capacitance is that associated with the bond pads and the geometrical design of the chip.

### 2.5.2 Measurement results

#### OE1077

This early GaAlInAs wafer was processed into buried ridge lasers. A typical light-current and efficiency plot is shown in figure 36. The threshold current of this device, which was 375 $\mu$ m long was 100mA; and it showed a differential quantum efficiency of only 10%. Since this is very much lower than is useful, and in fact was worse than earlier work, this materials system was abandoned in favour of the GaInAsP system.

#### OF634

This first full laser structure in the GaInAsP system was processed into both oxide stripe lasers, to assess basic materials quality, and was subsequently processed into buried ridge lasers to prove the overgrowth technology which would be required for subsequent high speed devices.

The light current characteristics under pulsed operation for a typical example of the oxide stripe lasers at temperatures from 20-80°C are shown in figure 37. Oxide stripe lasers are not expected to operate CW owing to their high threshold currents. The threshold current density for this (250x100 $\mu$ m active area) device was 2KA/cm<sup>2</sup> at 20°C, which is typical of bulk devices at this wavelength. The characteristic temperature for the same device (OF634/5) is derived from the plot in figure 38 of  $\log_e(I_{th})$  plotted against temperature. The  $T_0$  value is seen to be 40K for this device. The highest  $T_0$  observed from this wafer was 53K.

The buried ridge devices processed from this same wafer produced threshold currents of 20mA. The light current characteristic and the differential efficiency for a typical device is shown in figure 39. Operation at 60°C is illustrated in figure 40. It can be seen that the threshold current has risen to 45mA, still a very satisfactory figure.

#### OF653

These devices failed during the last stages of the processing, so no device testing was possible.

#### OF910 and OF912

These devices were processed into the full high speed structure. Typical light-current and efficiency plots for each wafer are shown in figures 41 and 42. The more promising in terms of power performance was OF912, having higher efficiency and showing less saturation in output power. This was therefore selected for the most detailed RF measurement and forms the basis for the deliverable devices.

### 2.5.3 Conclusions

The basic device materials quality, as measured using broad area lasers is of good quality with threshold current densities of  $<2\text{kA/cm}^2$ . The buried ridge lasers exhibited good linearity and high output powers, indicating that the structure of the devices was satisfactory. The SI substrate buried ridge devices showed lower thresholds than the N+ wafers, indicating further improvements in basic materials quality, or perhaps superior current confinement. Output powers of 30mW were achieved on some of these devices, again indicating good current confinement.

## 26 RF testing

Techniques for testing optoelectronic devices at high frequencies are less well developed than those for low frequency operation, since their exploitation at frequencies above 1-2GHz is only just commencing. In particular, it is important to ensure that test fixtures and connection methods do not compromise the performance of the devices under test. The devices fabricated

on this programme were bonded into a test fixture previously designed specifically for operation at high frequencies. This test fixture is also that on which the final deliverable devices were supplied. Section 2.6.1 describes this test fixture, 2.6.2 discusses the measurement technique, 2.6.3 describes the measurement results and 2.6.4 discusses the results.

#### 2.6.1 Test fixture and test methods.

The test fixture is shown schematically in figure 43. An SMA type RF connector supplies the signal and bias to a  $50\Omega$  microstrip line on an alumina substrate. The line is terminated with  $50\Omega$  resistor which is soldered directly across a short gap in the line. Very short bond-wires are used to connect from the end of the microstrip line to the n-contact of the laser. The laser is bonded onto either a metallized diamond, or onto a gold preform, which is in turn soldered onto a copper submount. Further short bond-wires are used to connect the p-contact of the laser to the heatsink with minimal inductance. Calculation of the effect of the parasitic elements in this construction were discussed in section 2.1. The light from the laser facet is collected by an anti-reflection coated Selfoc lens which is adjusted to give a satisfactory magnification of the output spot into a fiber.

#### 2.6.2 Measurement technique.

High speed operation of the lasers was characterized by modulating the laser in its test fixture with a sinusoidal small signal modulation super-imposed on a DC bias signal (introduced via an external bias Tee). The light was collected via an angle ended fibre (to minimize reflections) and was monitored with a wide band-width photodetector. The output from the photodetector was connected to a microwave network analyser which measured the RF power level as the frequency of the modulation was varied. This enabled plots of frequency response as a function of DC bias to be obtained on the network analyser. A schematic of the measurement system is shown in figure 44. The test fixture was characterized for its  $S_{11}$  reflection parameter, to ensure that it would not, in itself, limit the performance of the devices. The  $S_{11}$  parameter up to 20GHz is shown in figure 45.



### 2.6.3 Measurement results.

The technique described above was used to plot the small signal frequency response of two different length devices from the OF912 wafer.

Figure 46 shows the response of a 150 $\mu$ m chip (chip number 33), which forms one of the deliverable devices. The small signal response for a number of output powers is given. The power output is scaled from the values measured at the chip stage, so that the power being indicated is the true facet power, not that coupled through the lens and fibre. Similarly figure 47 shows the small signal response of the 250 $\mu$ m long device, again over a range of output powers, which forms the second deliverable device.

Figures 48 and 49 show  $f_r^2$ , the square of the resonance frequency, plotted against output power, as measured from the previous two graphs. This quantity is a measure of the carrier and photon lifetimes and is expected to be larger in MQW lasers owing to the increased gain-slope in these devices. The measured slopes for these two devices are 6.9 and 2.5GHz<sup>2</sup>/mW for the 150 $\mu$ m and 250 $\mu$ m lasers respectively. Very recent work at 1.55 $\mu$ m [25] has shown a strong dependence of the rate of evolution of  $f_r$  with power on the number of quantum wells, with our value of 2.5GHz<sup>2</sup>/mW being typical for a 250 $\mu$ m long device with 8 wells.

### 3. Conclusions

- MQW lasers at 1.3 $\mu$ m have been designed and fabricated in a high speed structure.
- High power operation (>20mW) and low threshold currents (<10mA) have been demonstrated.
- The MQW model has been validated and used to optimize barrier and well composition.
- Bandwidths of 10GHz at a power of 8mW have been demonstrated.
- A value of  $f_r^2/P$  of 6.9GHz<sup>2</sup>/mW for an 8 well 150 $\mu$ m long device has been achieved, equivalent to the highest reported for similar MQW structures with this number of wells.
- The value of  $f_r^2/P$  is less in the quantum well devices than that achieved in our bulk devices (12.5GHz<sup>2</sup>/mW see [24]), which are in line with other published works eg Olshansky, [26].
- The reduced value of  $f_r^2/P$  requires further investigation, in particular the effects of damping, possibly caused by inadequate carrier confinement.
- The effect of parasitic leakage currents in the BH structure requires investigation. We speculate that this not only acts to limit the output power and threshold values, but may contribute to reduced frequency response through diffusion capacitance.

### 4. Deliverables

Two devices have been delivered in test jigs, with chip lengths of 150 $\mu$ m and 250 $\mu$ m. Measurement data on these devices is included in this report. Connection data is given with the devices. The maximum recommended drive current is 100mA. The package case is to be biased positive. Both of the deliverable devices were taken from wafer OF912 and therefore have 8

quantum wells. The active region structure is shown in figure 27. Table 6, below, summarizes the deliverable devices.

Chip number	Chip Length $\mu\text{m}$	Current for 1mW ex lens	Frequency response figure number
33	150	25mA	46
62	250	20	47

Table 6 Summary of deliverable devices

## 5. Suggestions for further work

The main feature of this work which requires further experimental and theoretical investigation is the limit to the frequency response of the devices. There has been only limited work on MQW devices at  $1.3\mu\text{m}$  reported in the literature, and even less on high speed work.

A future work plan would include:

- Modelling of damping mechanisms in MQW devices
- Modelling and measurement of diffusion capacitance
- Further optimization of MQW growth
- Investigation of strained MQW devices, which are reported to show higher frequency responses
- Fabrication and assessment of devices to test the above theory and growth technologies.

A further activity which would be useful to make the resulting devices easier to use and assess for systems applications would be to develop a package suitable for operation to 20GHz. GEC Marconi already have a design for a fully hermetic package for operation to 10GHz, and we believe that this could be extended further.

## 6. References

- [1] N K Dutta S G Napholtz R Yen, T Wessel, T M Shen and N A Olsson, (1985) 'Long wavelength InGaAsP ( $\lambda \sim 1.3\mu\text{m}$ ) modified multiquantum well laser' Applied Physics Letters **46**(11) pp1036-1038
- [2] Y Sasai, J Ohya and M Ogura, (1989) 'Spectral Linewidth and resonant frequency Characteristics of InGaAsP/InP Multiquantum Well lasers' IEEE Journal of Quantum Electronics QE-25(4) pp662-667
- [3] Zh I Alferov, D Z Garbuzov, S V Zaitsev, A B Nivin, A V Ovchinnikov and I S Tsarov (1987) 'Quantum well InGaAsP/InP separate-confinement double heterostructure lasers emitting at  $\lambda = 1.3\mu\text{m}$  ( $J_{th} = 410 \text{ A/cm}^2$ ,  $T = 23^\circ\text{C}$ )' Soviet Physics of Semiconductors (1987) **21**(5) pp503-506
- [4] R M Ash, D J Robbins and J Thompson (1989) 'GRIN-SCH AlGaInAs/InP quantum well lasers emitting at 1300nm' Electronics Letters **25** pp1530-1531
- [5] H Ishiguro, T Kawabata and S Koike, (1988) 'InGaAsP multiple quantum well lasers with planar buried heterostructure prepared by metalorganic chemical vapor deposition' Applied Physics Letters **52**(25) pp.2099-2101.
- [6] T Kawabata, H Ishiguro and S Koike (1988) 'Metalorganic chemical vapor deposition of InGaAsP/InP layers and fabrication of  $1.3\mu\text{m}$  planar buried heterostructure lasers', Journal of Applied Physics, **64**(7), pp 3684-3688,
- [7] A Kasukawa, Y Imajo and T Makino, (1989) ' $1.3\mu\text{m}$  GaInAsP/InP heterostructure graded index separate confinement multiple quantum well (BH-GRIN-SCH-MQW) lasers entirely grown by metalorganic chemical vapor deposition (MOCVD)', Electronics Letters, **25**(2), pp104-105
- [8] A Kasukawa, N Matsumoto, I J Murgatroyd, Y Imajo, H Okamoto and S Kashiwa, (1989) '100mW output power GaInAsP Buried graded index separate confinement heterostructure multiple quantum well (GRIN-SCH MQW) laser diodes entirely grown by MOCVD', Proceedings of ECOC 1989, pp. 260-263.

- [9] A Kasukawa, I J Murgatroyd, Y Imajo N Matsumoto, T Fukushima, H Okamoto and S Kashiwa, (1989) 'High quantum efficiency, high output power,  $1.3\mu\text{m}$  GaInAsP buried graded index separate confinement heterstructure multiple quantum well (GRIN-SCH-MQW) laser diodes', Japanese.Journal.of Applied. Physics. 28(4) ppL661-L663
- [10] M J Ludowise, T R Ranganath and A Fischer-Colbrie, (1990) 'Continuously graded-index separate confinement heterostructure multiquantum well  $\text{Ga}_{1-x}\text{In}_x\text{As}_{1-y}\text{P}_y/\text{InP}$  ridge waveguide lasers grown by low-pressure metalorganic chemical vapor deposition with lattice matched quaternary wells and barriers", Applied Physics Letters, 57(15), pp 1493-1495
- [11] L Goldstein, 'Optoelectronic devices by GSMBE', (1990) Journal of Crystal Growth, 105, pp 93-96
- [12] Final report F19628-85-C-0172 'Research and development for laser sources based on quantum well structures fabricated in the InP alloy system' (1988)
- [13] P D Greene, J E A Whiteaway, G D Henshall, R W Glew, C M Lowney, B Bhumbra and D J Moule, (1991) 'Optimisation and comparison of InP-based quantum well lasers incorporating InGaAlAs or InGaAsP alloys' Proceedings of the International Symposium on GaAs and Related Compounds (Jersey:1990), Institute of Physics Conference Series 112 Chapter 8 pp555-560
- [14] B Soucail, P Voisin, M Voos, D Rondi, J Nagle and B de Crémoux, (1990) 'Optical investigations of the band offsets in an InGaAs-InGaAsP-InP double-step heterostructure' Semiconductor Science and Technology 5 pp918-920
- [15] J Nagle and C Weisbuch, (1988) 'Optimisation of GaInAs/GaInAsP/InP and GaInAs/AlInAs/InP quantum well lasers' Proceedings of the International Symposium on GaAs and related Compounds Heraklion : Greece 1987), Inst. Phys. Conf. Ser. No.91 Ch 7 pp617-620

- [16] J Nagle, S Hersee, M Krakowski, T Weil and C Weisbuch (1986) 'Threshold current of single quantum well lasers : The role of the confining layers' (1986) *Applied Physics Letters*. 49(20) pp1325-1327
- [17] A I Kucharska and D J Robbins (1990) 'Lifetime broadening in GaAs-AlGaAs Quantum well lasers' *IEEE Journal of Quantum Electronics* QE-26(3) pp443-448
- [18] R Olshansky, C B Su, J Manning and W Powazinik, (1984) 'Measurement of Radiative and Nonradiative Recombination Rates in InGaAsP and AlGaAs light sources' *IEEE Journal of Quantum Electronics* QE-20(8) pp838-854
- [19] B Sermage, J P Heritage and N K Dutta (1985) 'Temperature dependence of carrier lifetime and Auger recombination in 1.3 $\mu$ m InGaAsP' *Journal of Applied Physics* 57(12) pp5443-5449
- [20] E Wintner and E P Ippen, (1984) 'Nonlinear carrier dynamics in Ga<sub>x</sub>In<sub>1-x</sub>As<sub>y</sub>P<sub>1-y</sub> compounds' *Applied Physics Letters* 44(10) pp999-1001
- [21] C H Henry, R A Logan, F R Meritt and J P Luongo, (1983) 'The effect of intervalence band absorption on the thermal behaviour of InGaAsP lasers' *IEEE Journal of Quantum Electronics*. QE-19(6) pp947-952
- [22] M-C Amann and W Thulke, (1989), "Current confinement and leakage currents in planar buried ridge structure laser diodes on n substrate", *IEEE Journal of Quantum Electronics*. QE 25(7) pp1595-1602.
- [23] A P Webb and J A Smith, (1988), "Applications of in-situ SIMS during processing of electronic materials", *Surface and Interface Analysis*, Vol 12, pp303-308.
- [24] R M Ash, G G Jones and P H Fell, (1990), "High speed self aligned 1300nm buried ridge laser suitable for integration", *IEE Proc Vol 137 Pt. J, No.5*, pp315-317.
- [25] M C Tatham, C P Seltzer, S D Perrin and D M Cooper, (1991), "Frequency response and differential gain in strained and unstrained InGaAs/InGaAsP quantum well lasers", *Electronics Letters* Vol. 27, No. 14, pp1278-1280.

- [26] R Olshansky, P Hill, V Lanzisera and W Powazanik, (1987), "Frequency reponse of 1.3 $\mu$ m InGaAsP high speed semiconductor lasers", IEEE Journal of Quantum Electronics QE-23(9) pp1410-1418.
  
- [27] R M Ash, D J Robbins, P Charles, G G Jones, P H Fell, A K Wood and N Carr, (1991), "A high speed low capacitance laser structure for integration", Proceedings of 3rd International Conference on Indium Phosphide and Related compounds, pp122-125.

# Figures

1-49



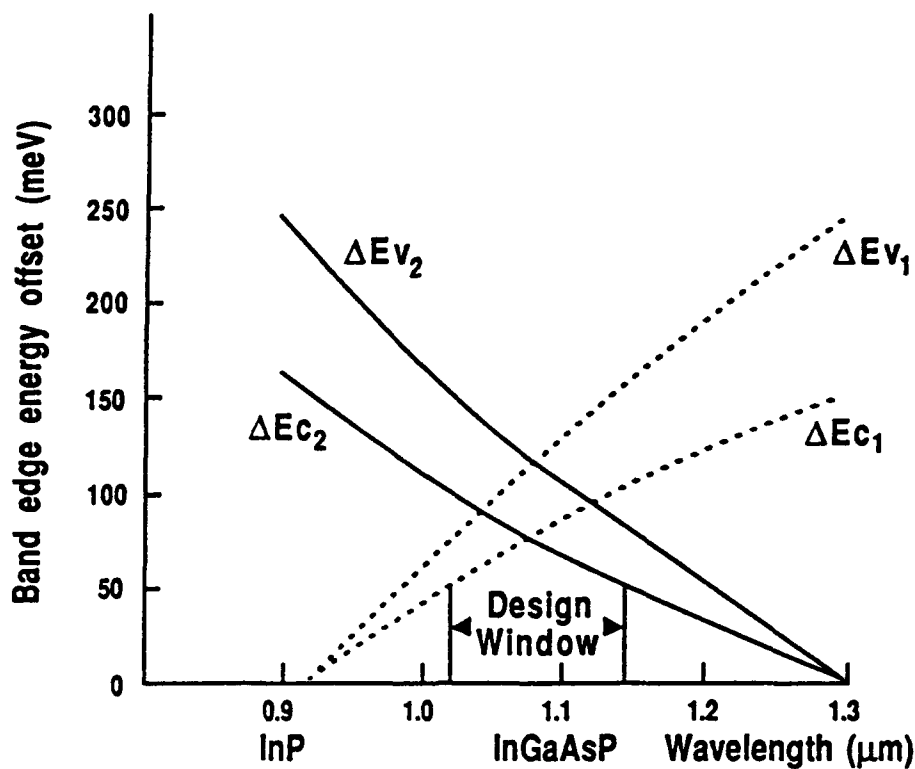


Figure 1 Band edge offsets for InP to quaternary guide,  $\Delta E_{c1}$ ,  $\Delta E_{v1}$ , and guide to 1.3 μm quaternary well,  $\Delta E_{c2}$ ,  $\Delta E_{v2}$ .

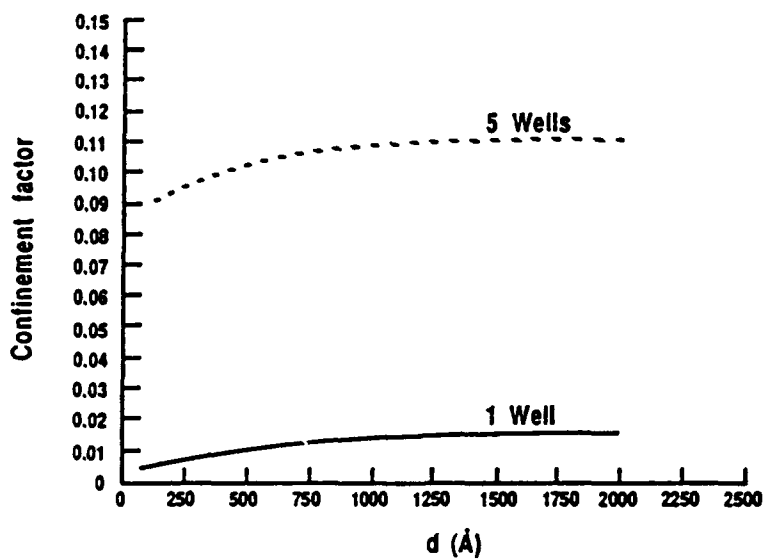


Figure 2 Optical confinement factor as a function of outer well dimensions.

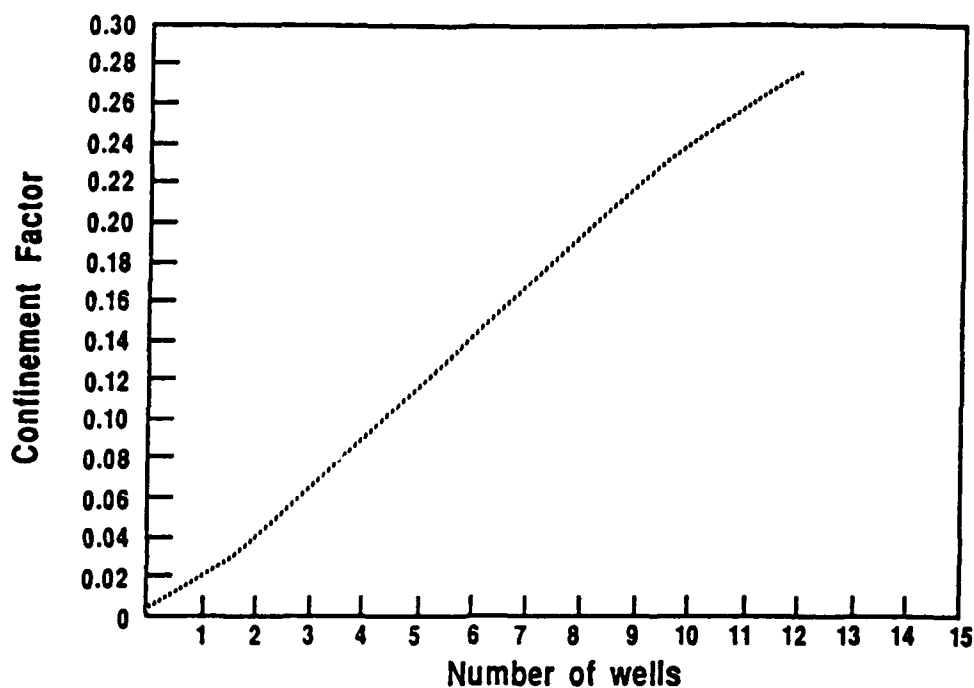


Figure 3 Optical confinement factor as a function of well number for  $d=1000\text{\AA}$  and a  $1.07\mu\text{m}$  quaternary guide layer.

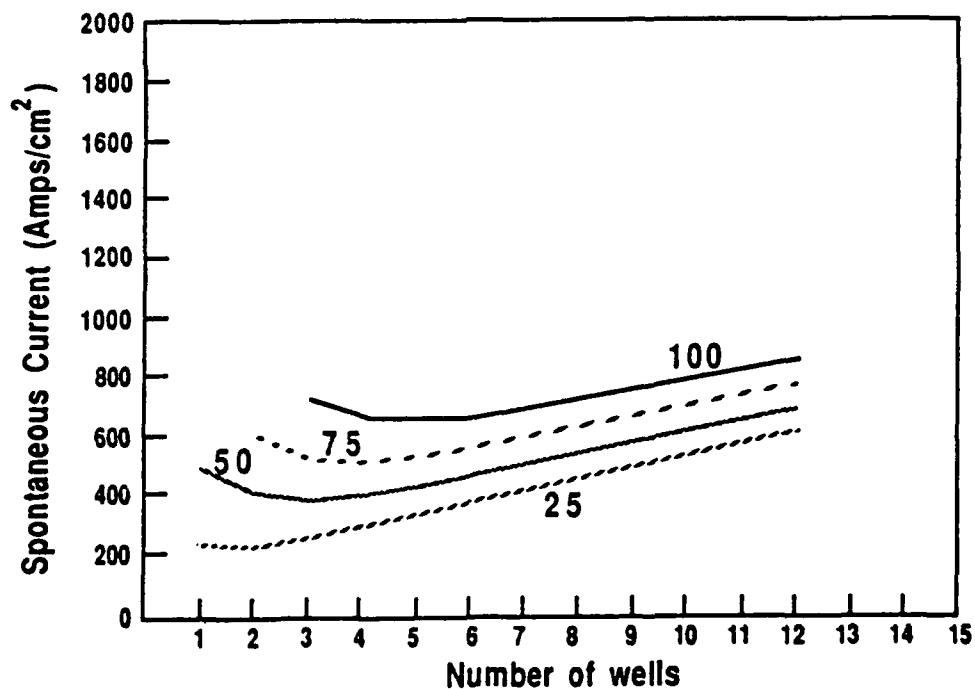


Figure 4 Calculated spontaneous emission current at threshold for a total loss of 25,50,75, and  $100\text{cm}^{-1}$ .

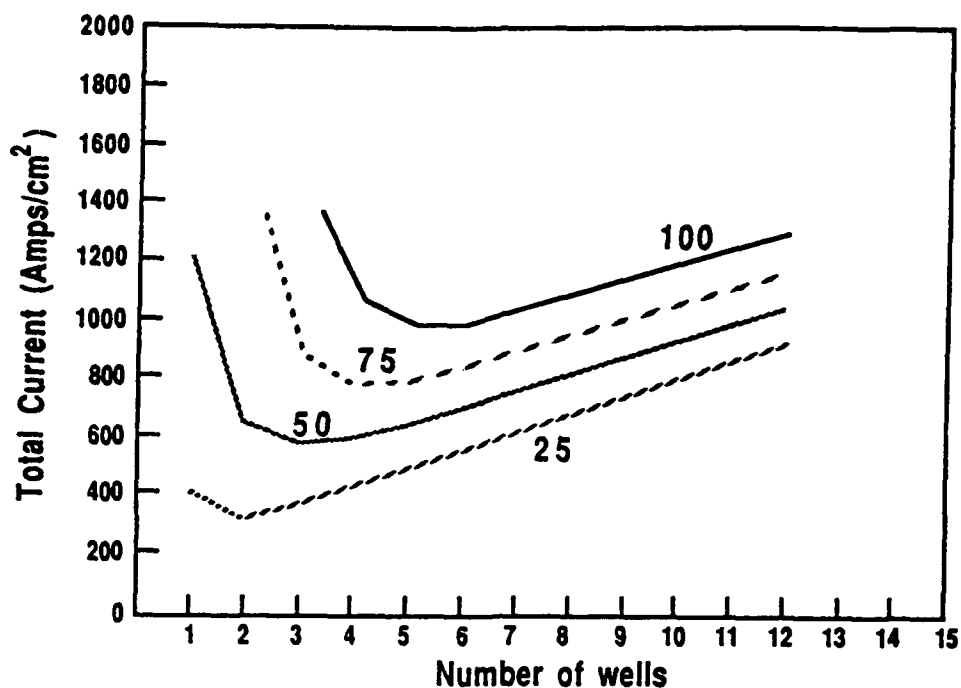


Figure 5 Total threshold current (including Auger recombination) for a total cavity loss of 25,50,75 and 100cm<sup>-1</sup>.

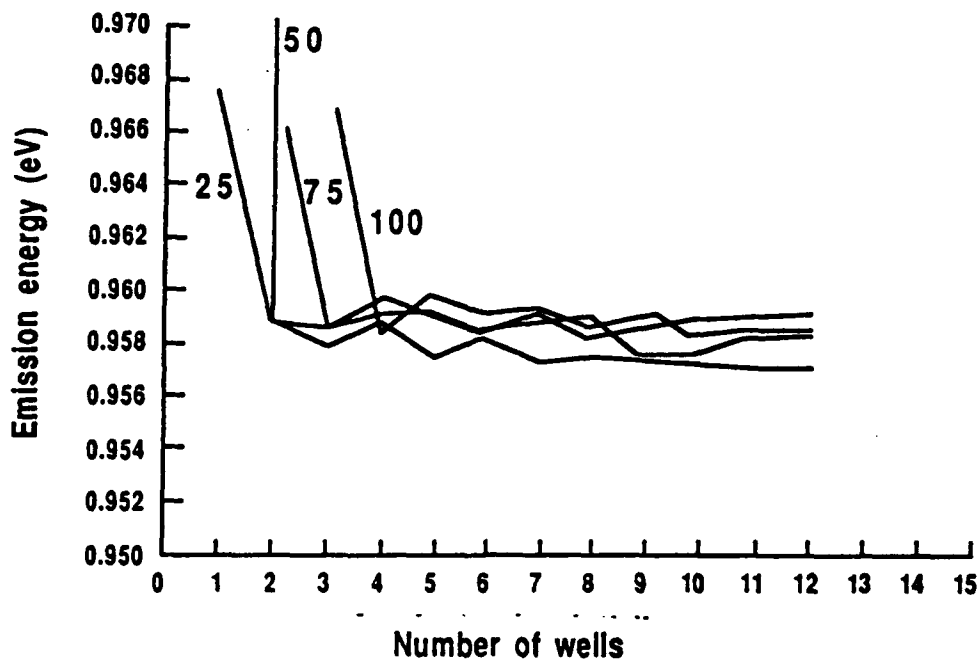


Figure 6 Calculated lasing emission energy.

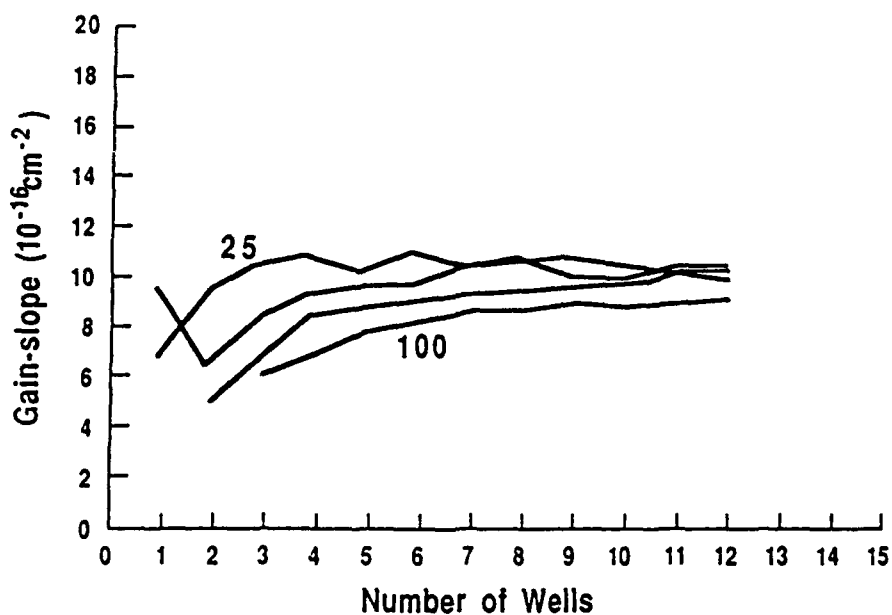


Figure 7 Gainslope at threshold as a function of the number of wells.

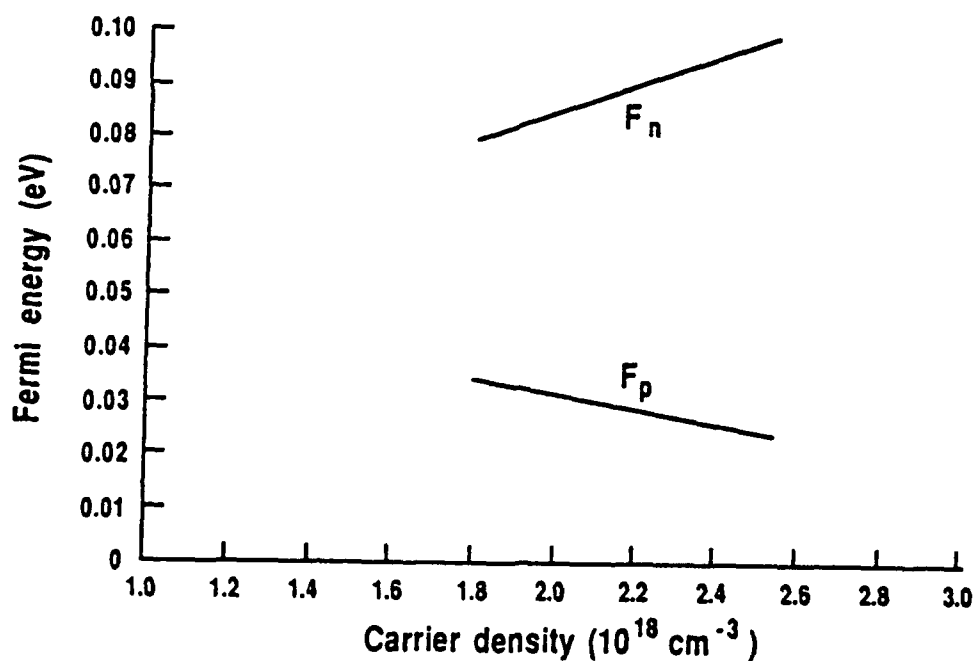


Figure 8 The Fermi energy as a function of carrier density for electrons ( $F_n$ ), and holes ( $F_p$ ).

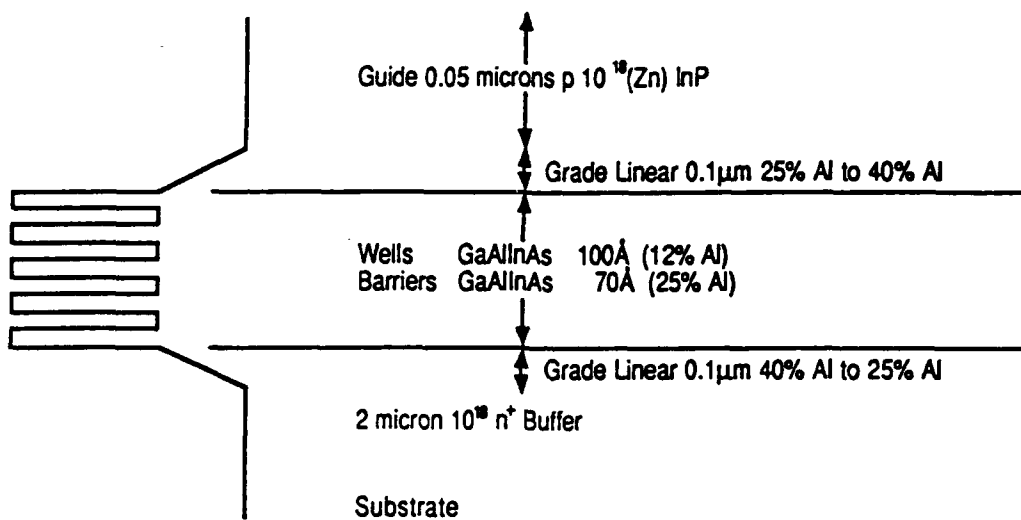


Figure 9 GaAlInAs MQW laser active layer specification

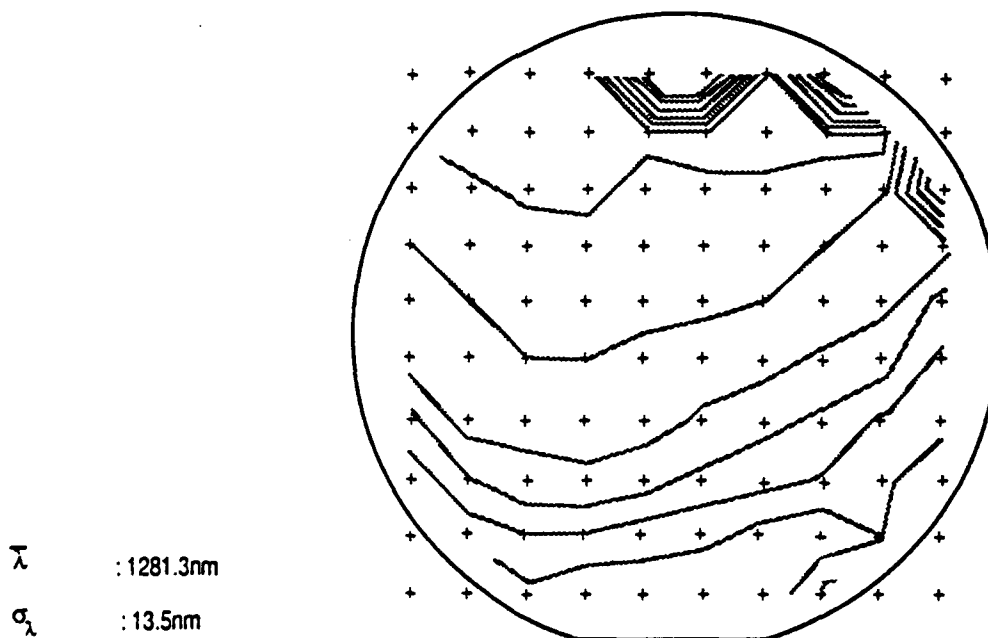


Figure 10 Photoluminescence map of OE1077 GaAlInAs MQW laser (5nm contours)

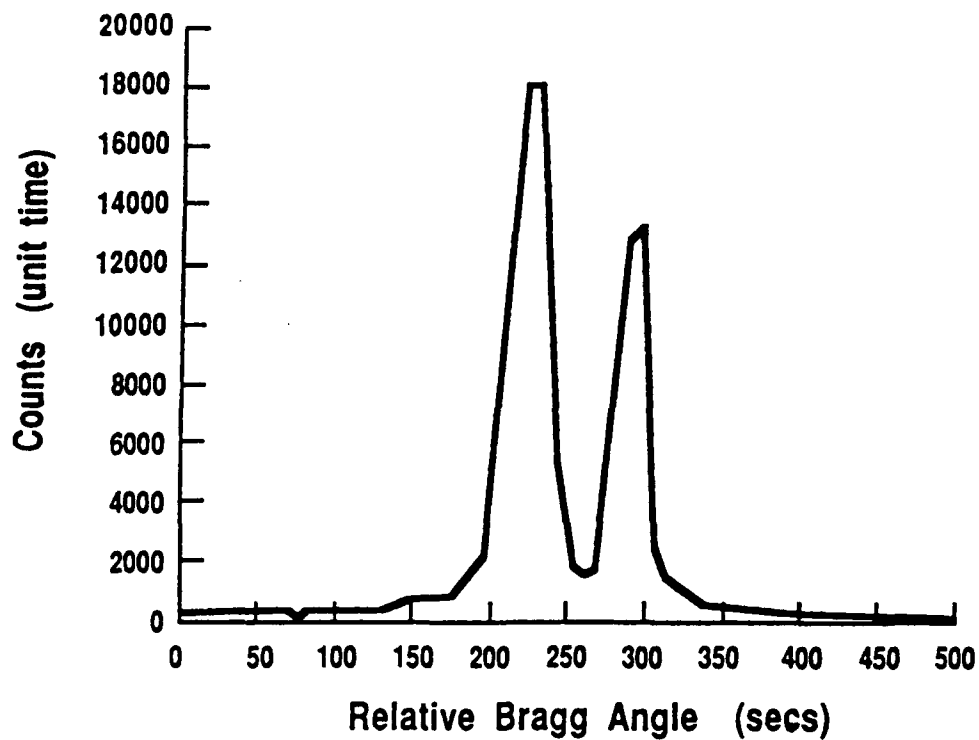


Figure 11 Double crystal X-ray diffractogram for bulk  $\lambda=1.07\mu\text{m}$  GaInAsP layer

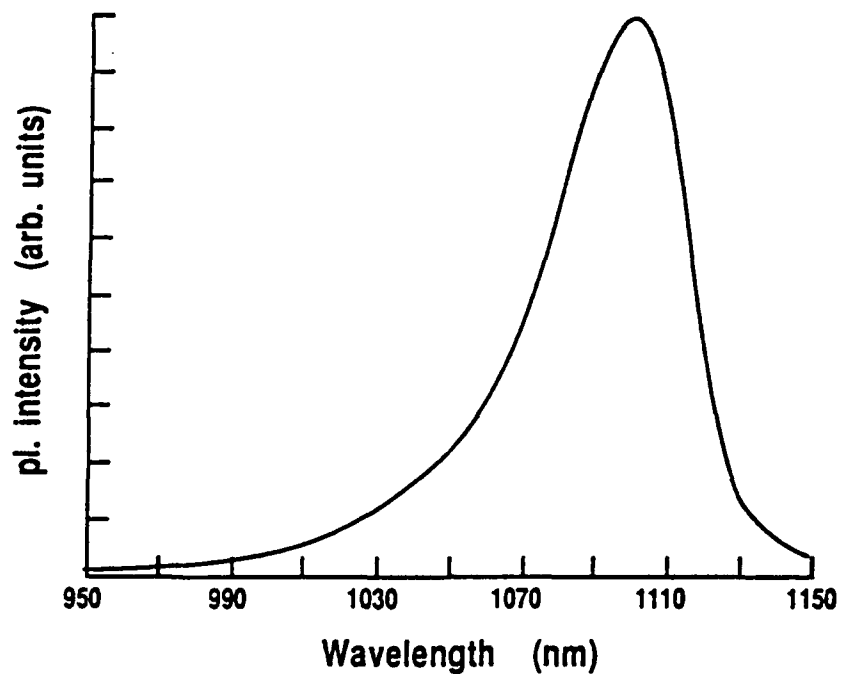


Figure 12 Photoluminescence spectrum for  $\lambda=1.07\mu\text{m}$  bulk GaInAsP layer

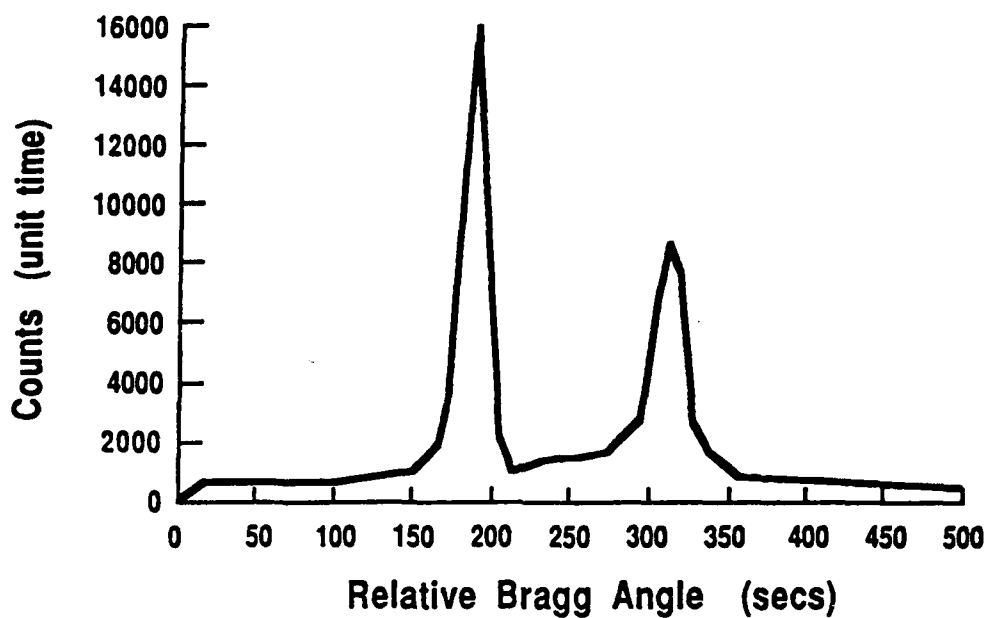


Figure 13 Double crystal X-ray diffractogram for bulk  $\lambda=1.3\mu\text{m}$  GaInAsP layer

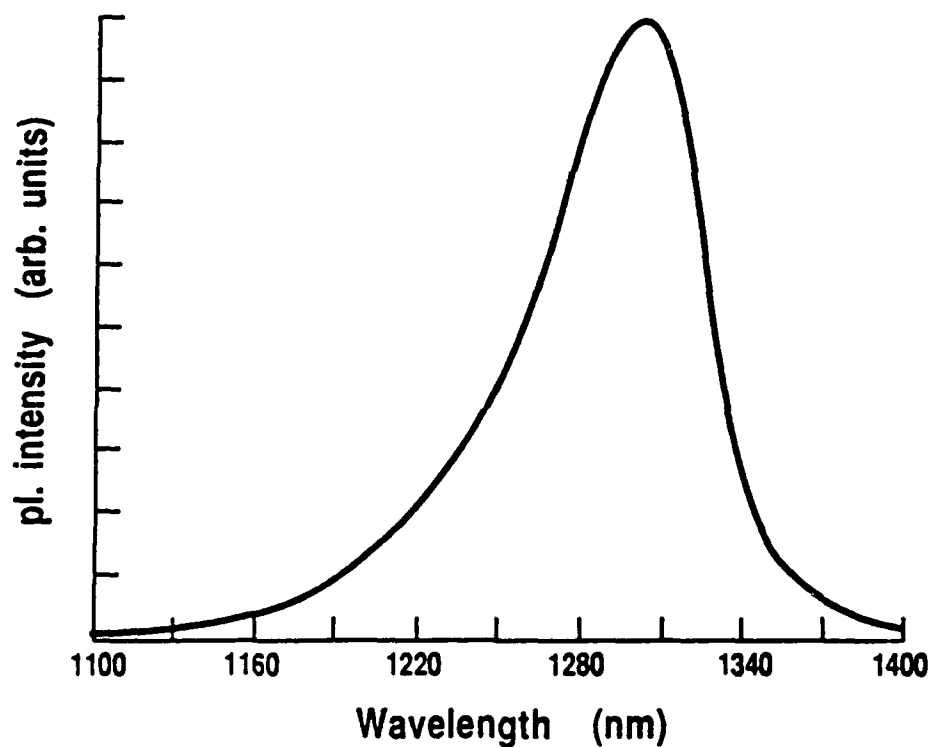


Figure 14 Photoluminescence spectrum for  $\lambda=1.3\mu\text{m}$  bulk GaInAsP layer

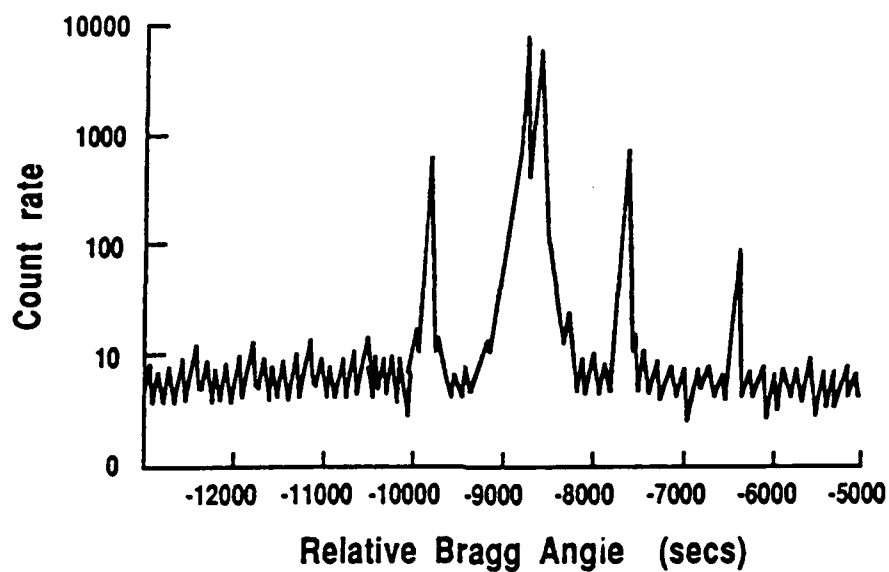


Figure 15 Double crystal X-ray diffractogram for a 90 period MQW test structure

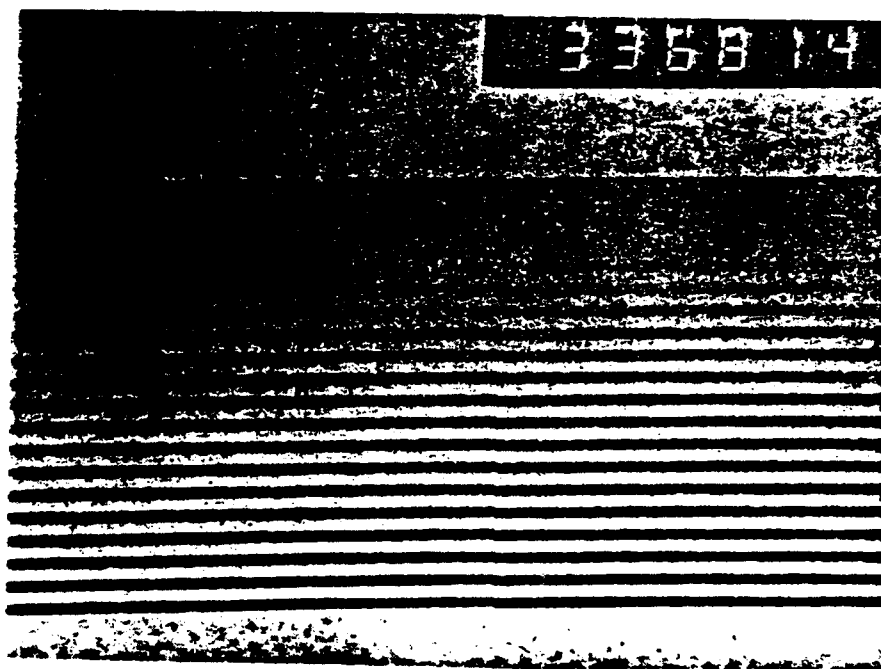


Figure 16 TEM cross sectional view of a 15 well MQW test structure



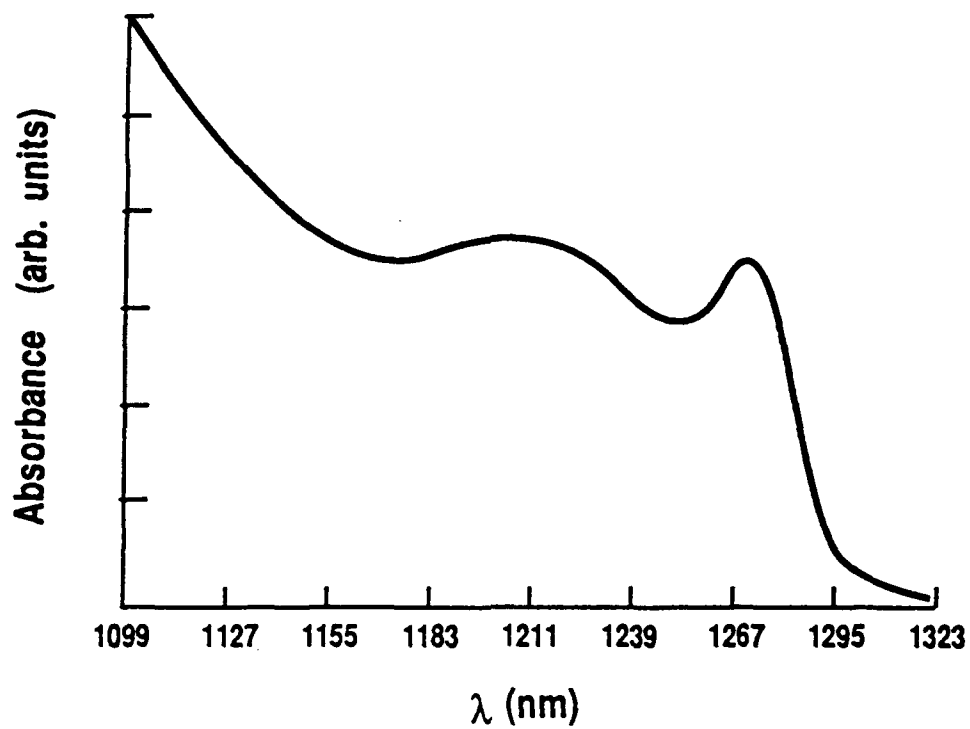


Figure 17 Absorbance spectrum of a 30 period MQW test structure

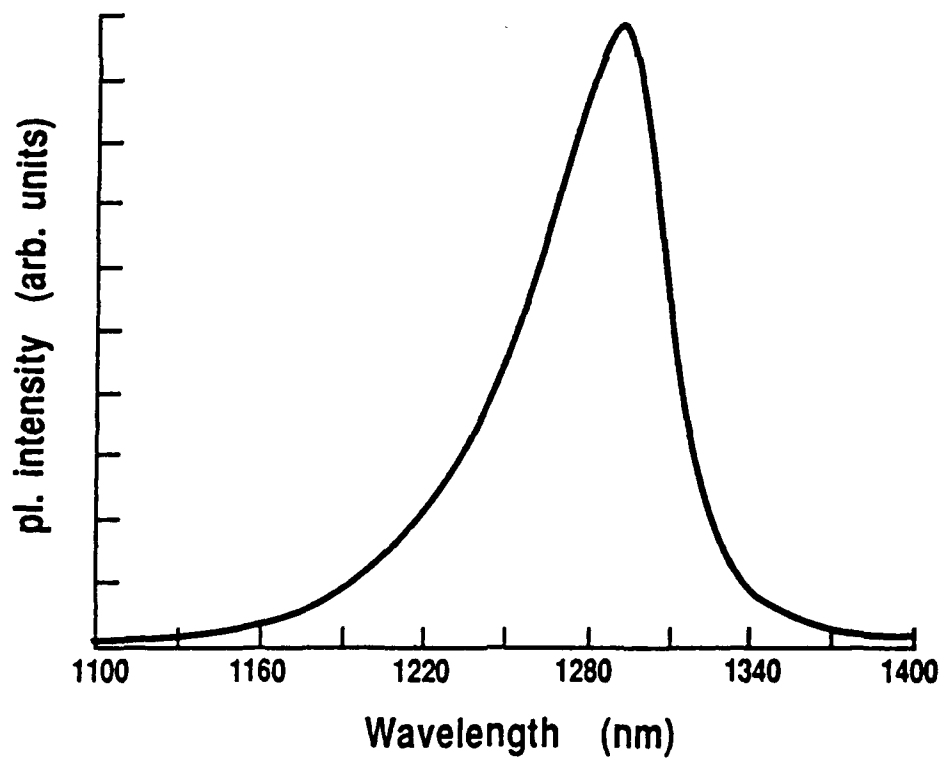


Figure 18 Photoluminescence spectrum for a 30 period MQW test structure (OF621)

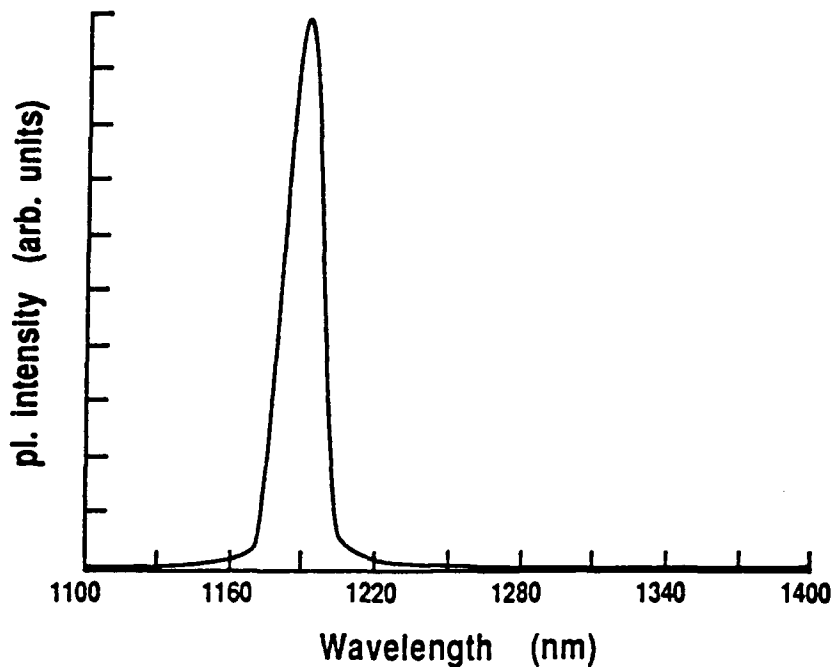


Figure 19 Low temperature (10K) photoluminescence spectrum for a 30 period MQW test structure (OF623)

	Thickness	Doping	Composition
	500 Å	$3 \times 10^{17}$ (Zn)	InP
	100 Å	$3 \times 10^{17}$ (Zn)	1.07 - GaInAsP
	900 Å	NUD	1.07 - GaInAsP
	5 Wells 100 Å	NUD	1.3 - GaInAsP
	4 Barriers 100 Å	NUD	1.07 - GaInAsP
	900 Å	NUD	1.07 - GaInAsP
	100 Å	$10^{18}$ (Se)	1.07 - GaInAsP
	2 microns	$2 \times 10^{18}$ (Se)	InP

Figure 20 Specification of 5 well GaInAsP MQW laser source wafer (OF634)

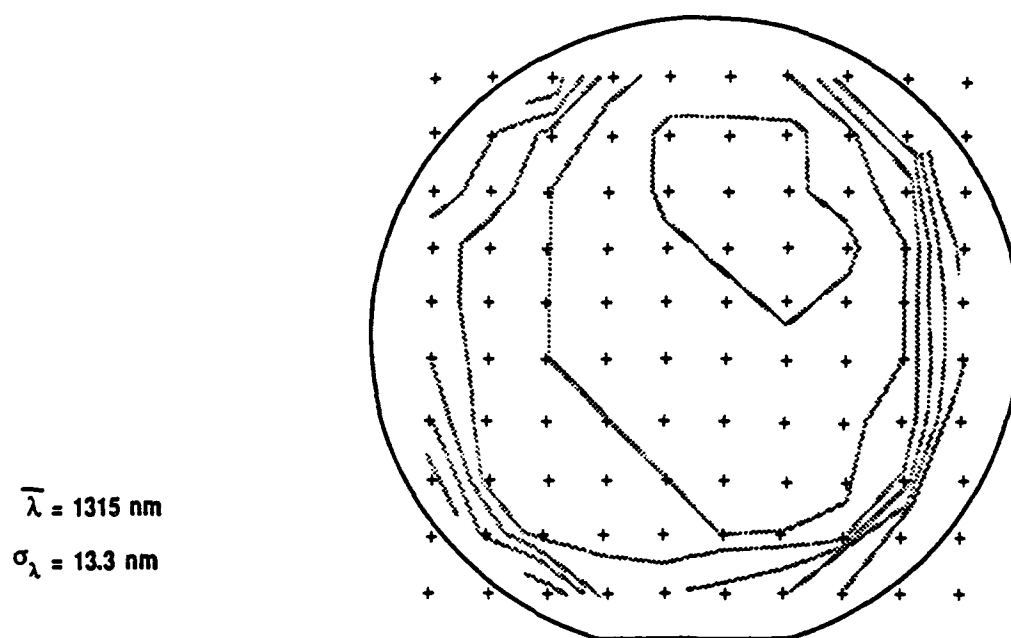


Figure 21 Photoluminescence map of OF634 (5nm contours)

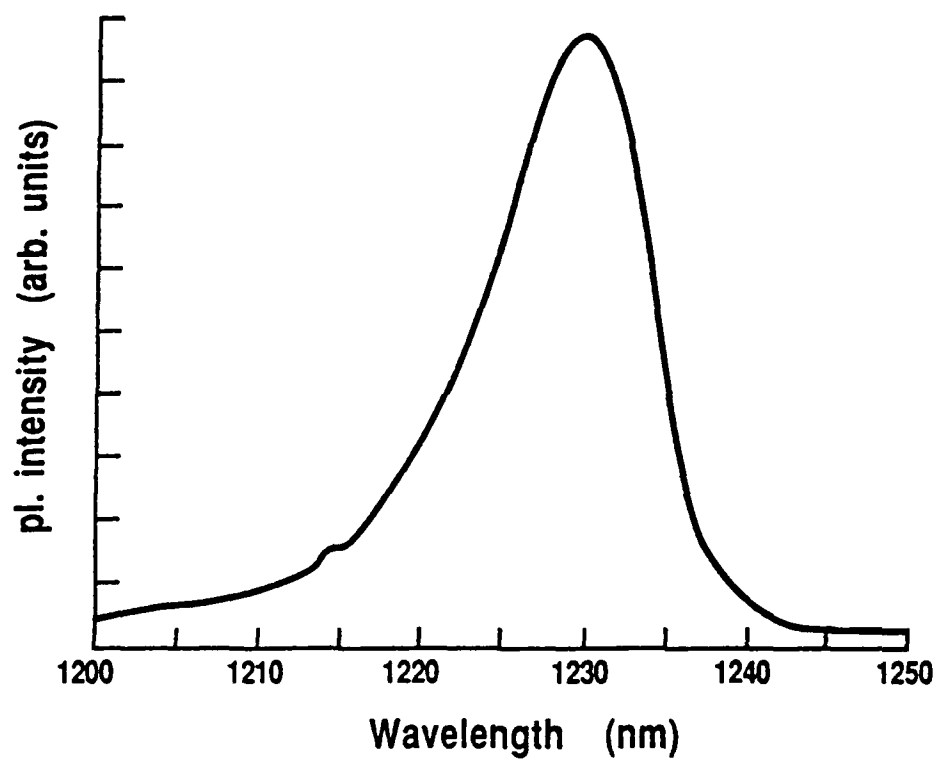


Figure 22 Low temperature (10K) photoluminescence spectrum for OF634

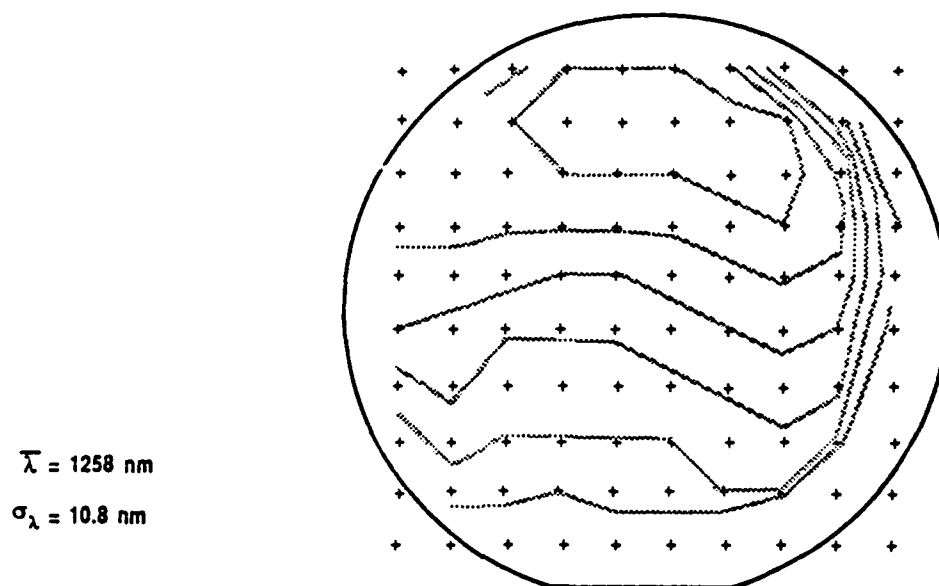


Figure 23 Photoluminescence map of OF653 (5nm contours)

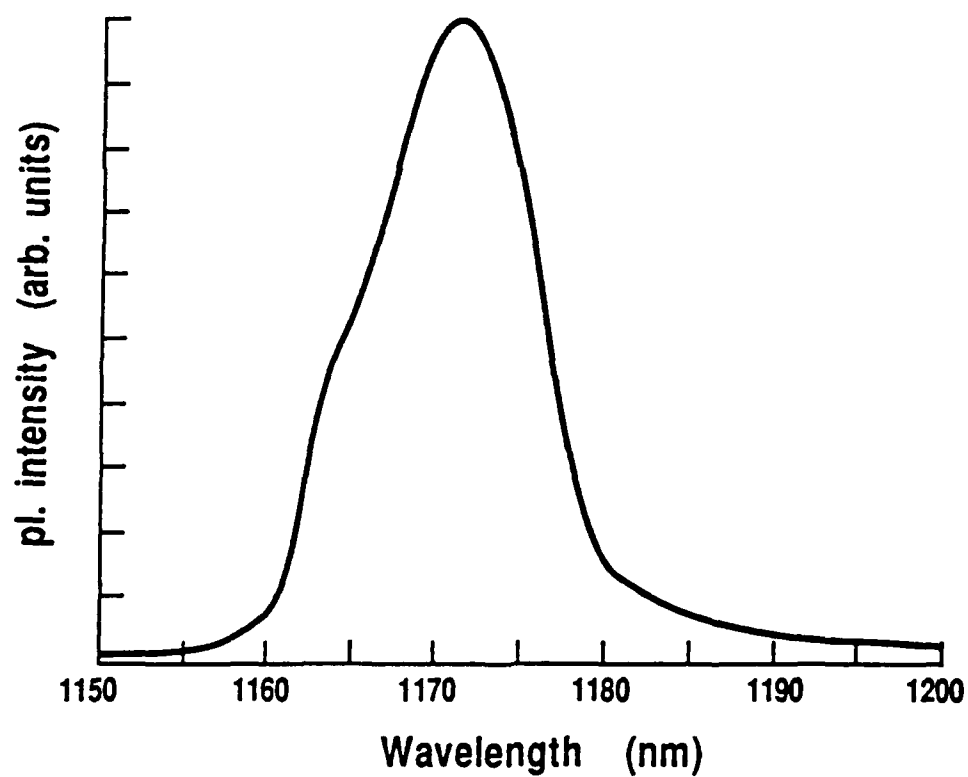


Figure 24 Low temperature (10K) photoluminescence spectrum for OF653

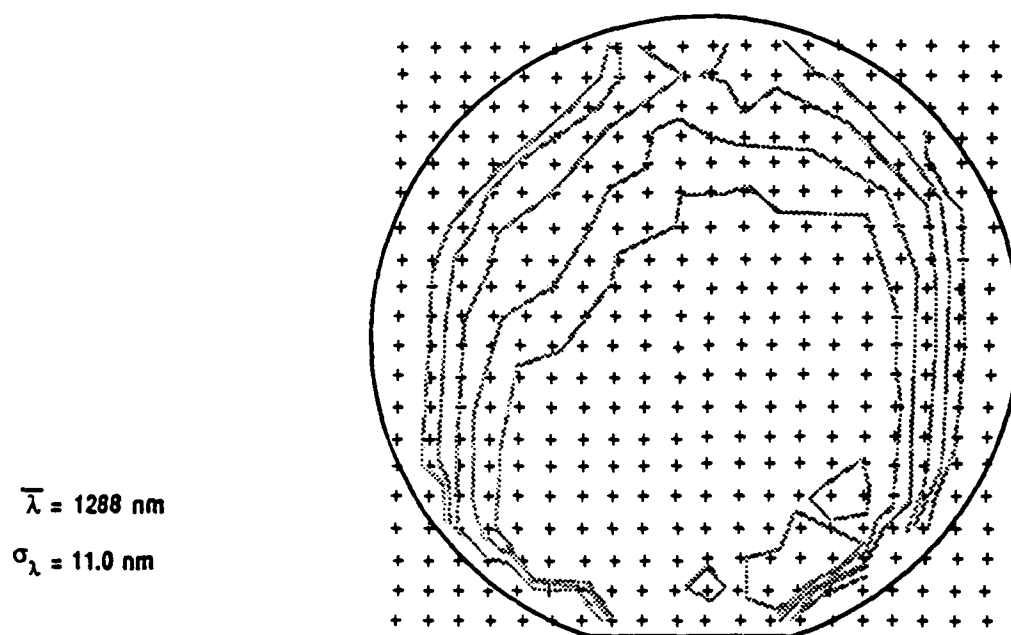


Figure 25 Photoluminescence map of OF910 (5nm contours)

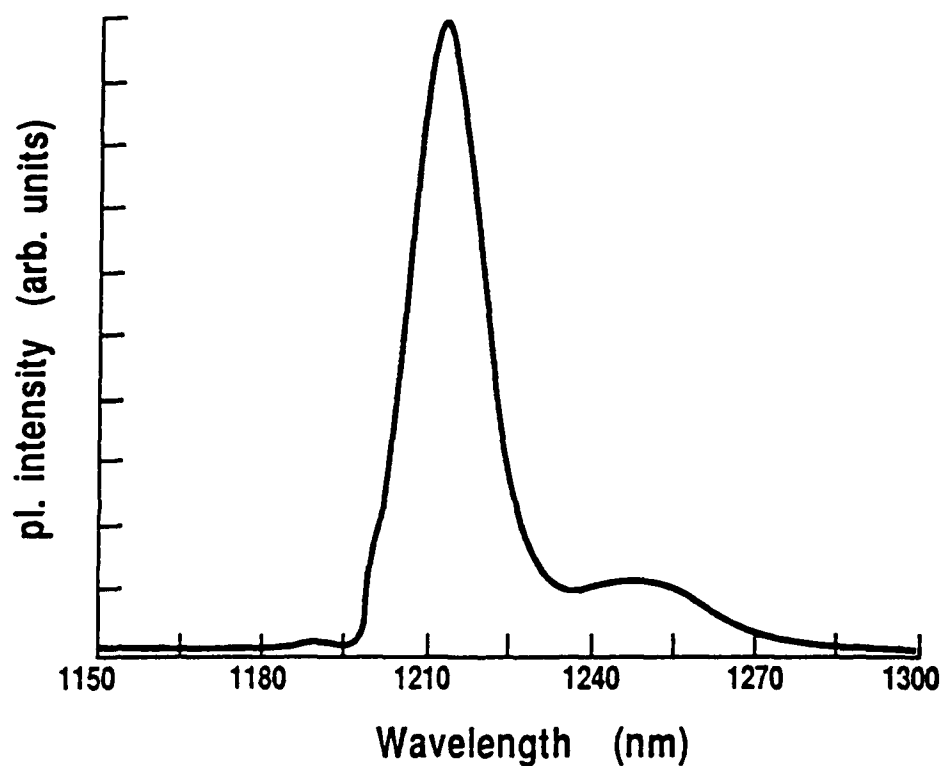


Figure 26 Low temperature (10K) photoluminescence spectrum for OF910

Thickness	Doping	Composition
500 Å	$3 \times 10^{17}$ (Zn)	InP
100 Å	$3 \times 10^{17}$ (Zn)	1.07 GaInAsP
900 Å	NUD	1.07 GaInAsP
8 Wells 100 Å	NUD	1.3 GaInAsP
7 Barriers 100 Å	NUD	1.07 GaInAsP
900 Å	NUD	1.07 GaInAsP
100 Å	$10^{18}$ (Se)	1.07 GaInAsP
2 microns	$2 \times 10^{18}$ (Se)	InP

Figure 27 Specification of 8 well GaInAsP MQW laser source wafer (OF912)

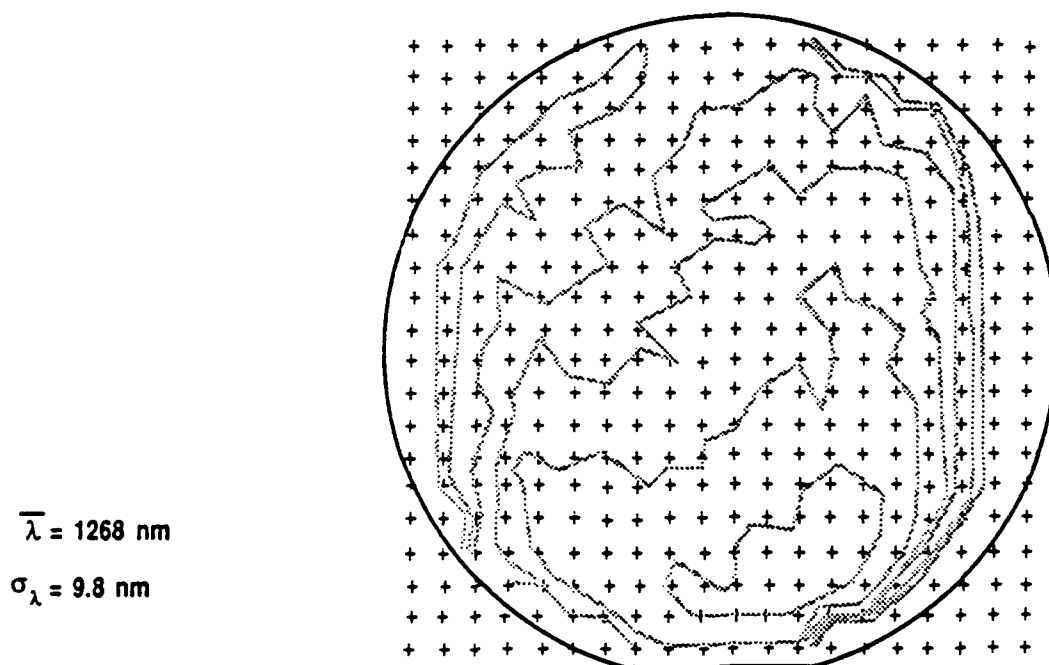


Figure 28 Photoluminescence map of OF912

Use, duplication or disclosure of data contained on this sheet is subject to the restrictions on the title page of this document.

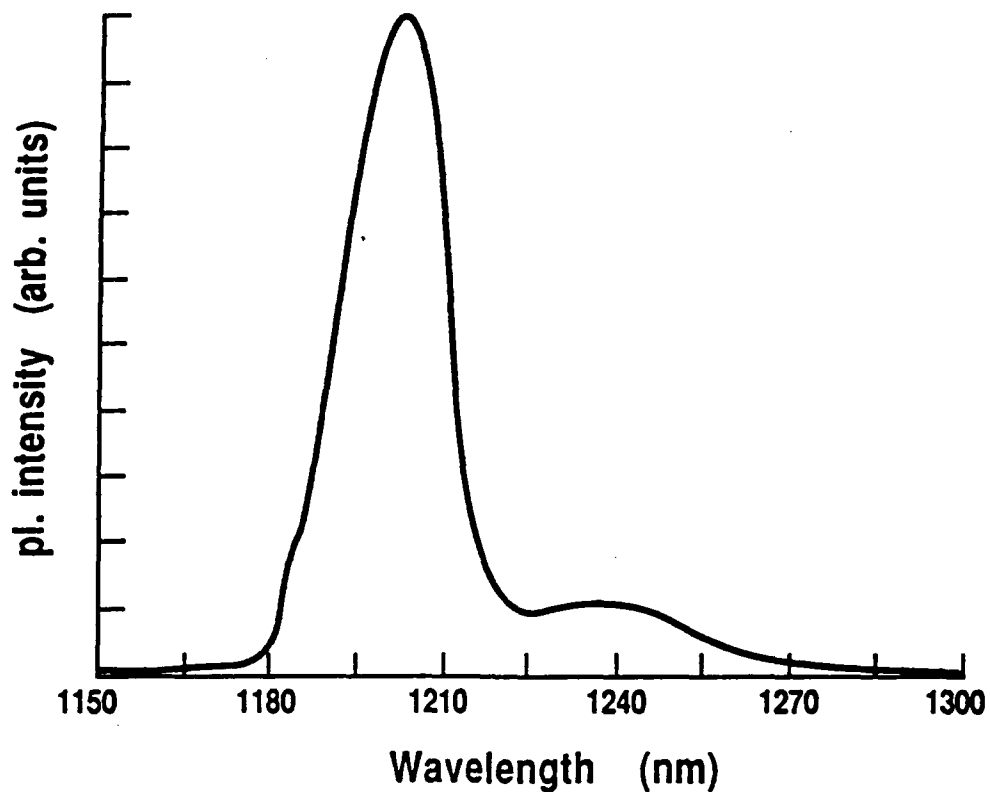


Figure 29 Low temperature (10K) photoluminescence spectrum for OF912

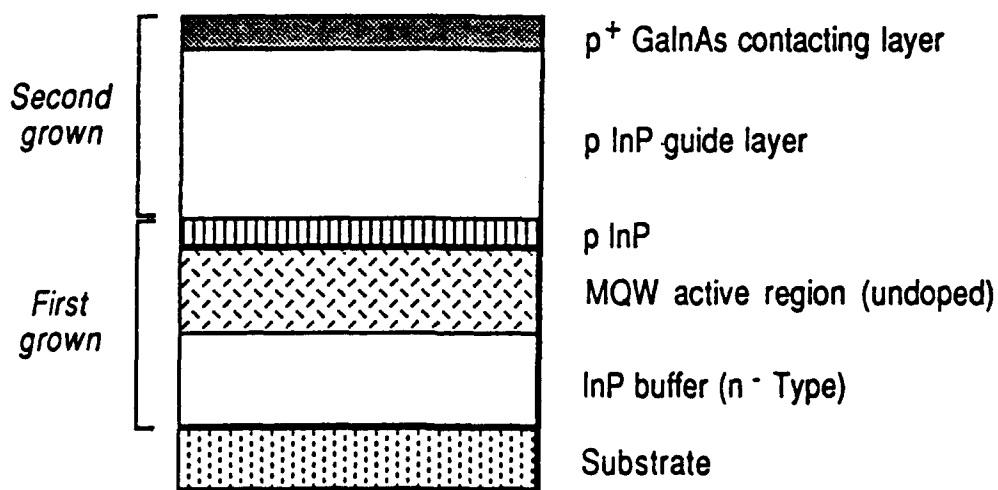


Figure 30 Layer structure for oxide stripe broad area lasers

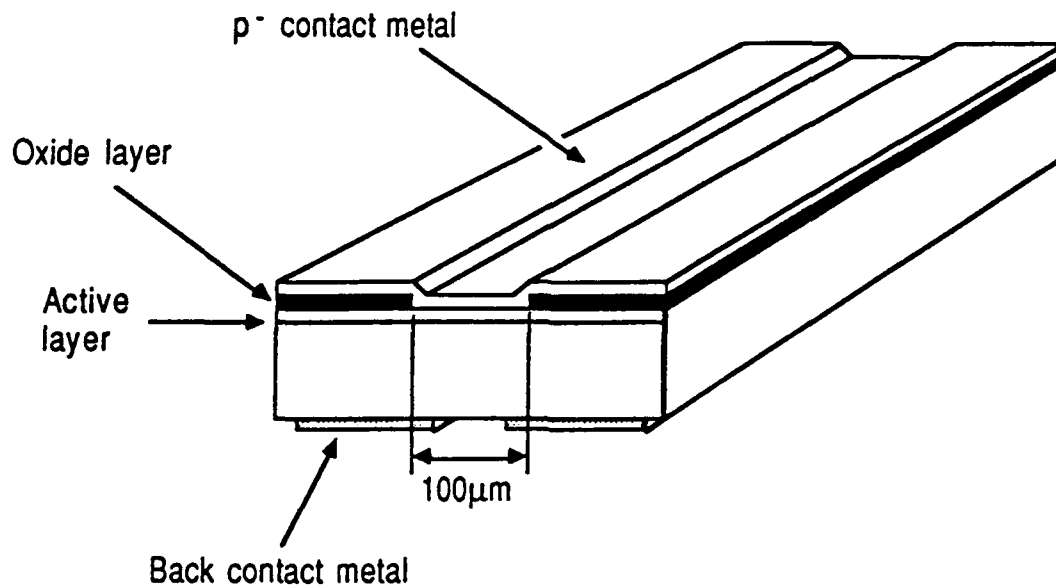


Figure 31 Schematic of broad area laser structure

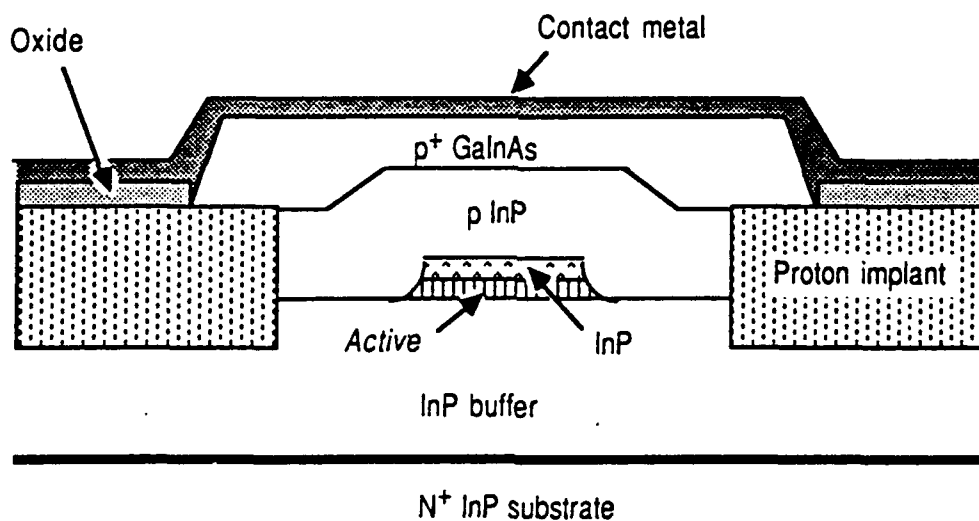


Figure 32 Schematic of buried ridge laser structure



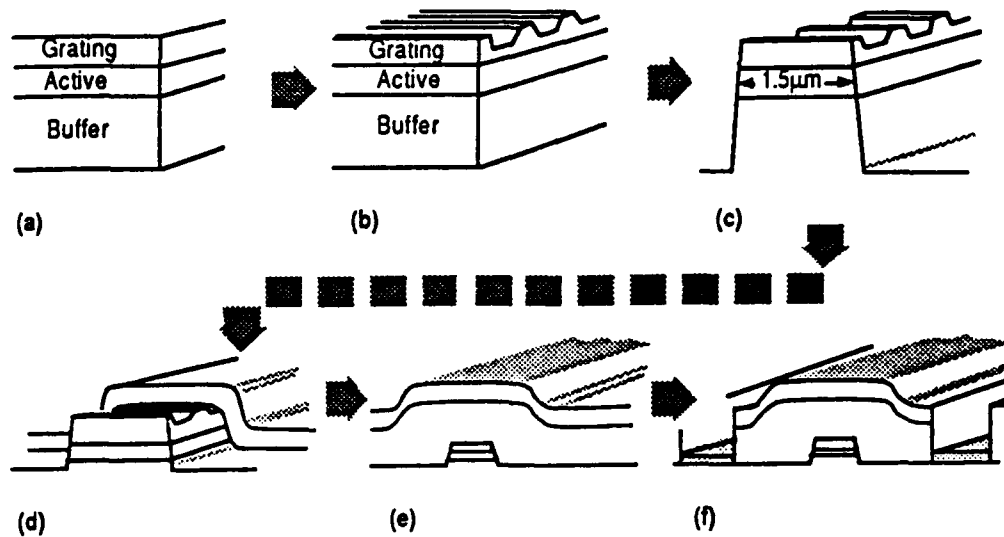


Figure 33 Schematic showing fabrication sequence for SI substrate BR lasers

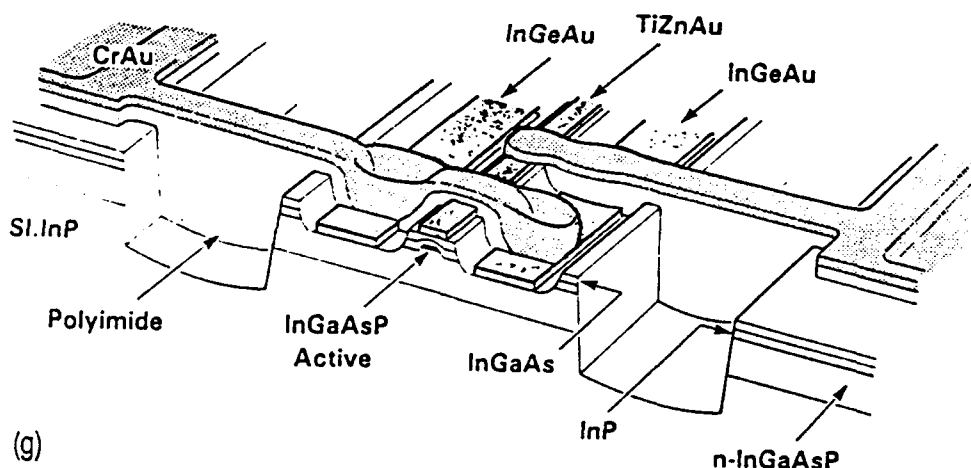


Figure 34 Schematic of completed SI substrate BR laser

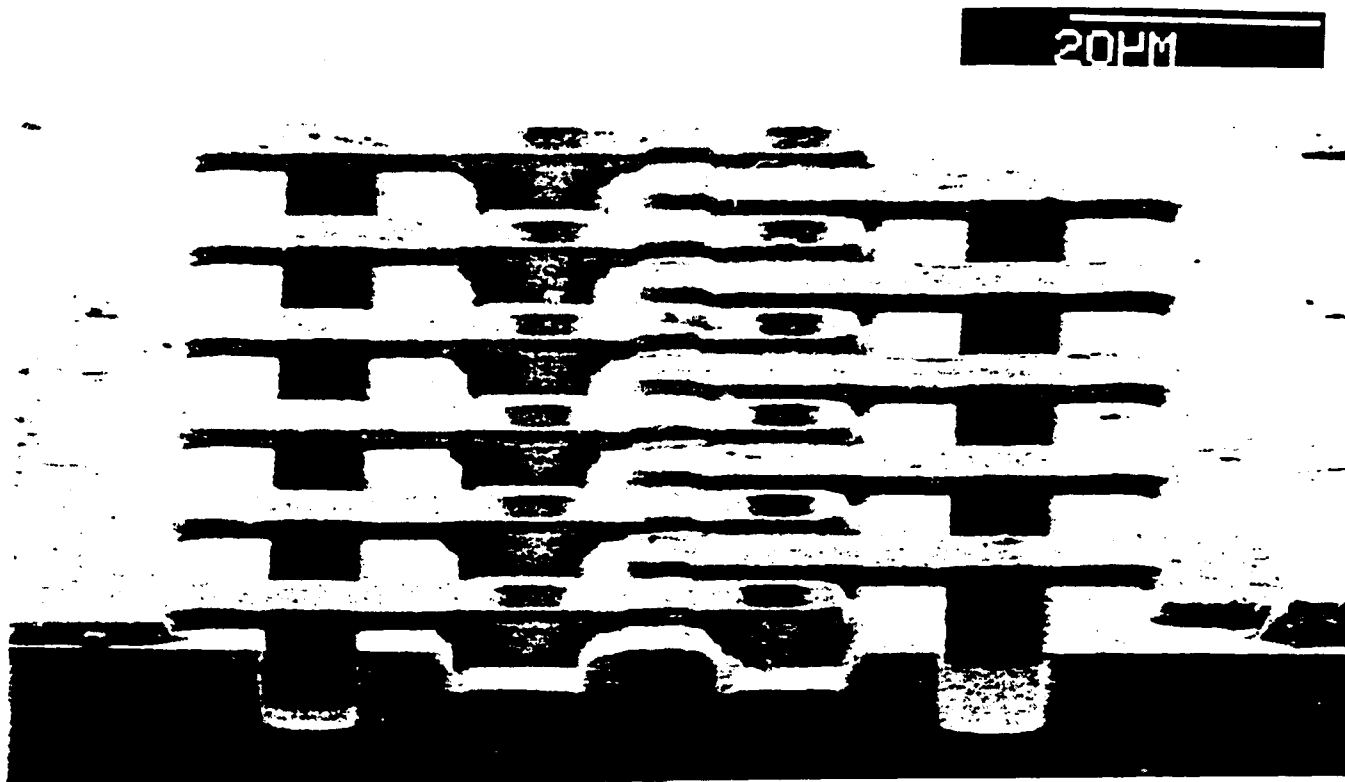


Figure 35 Electron micrograph of completed SI substrate BR laser

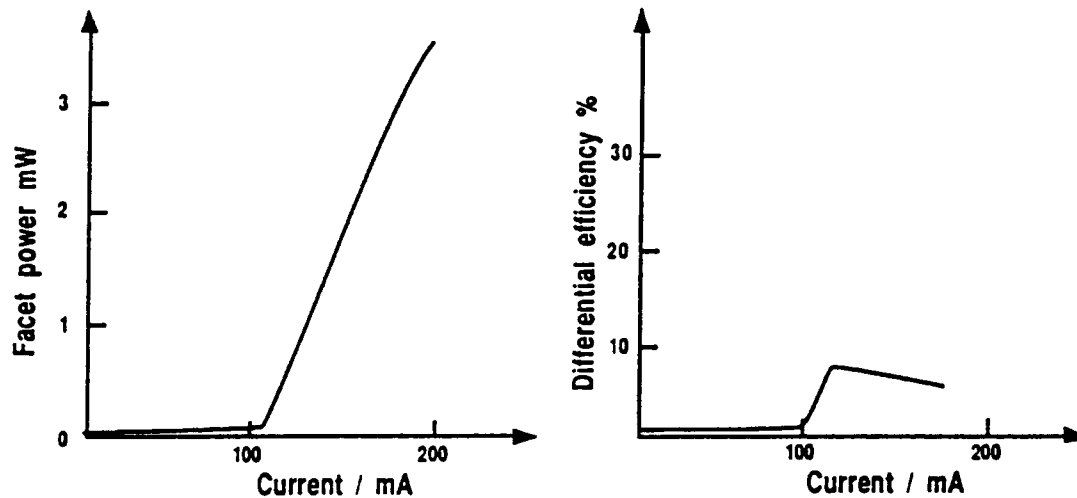


Figure 36 Light current and efficiency plot of GaAlInAs MQW laser

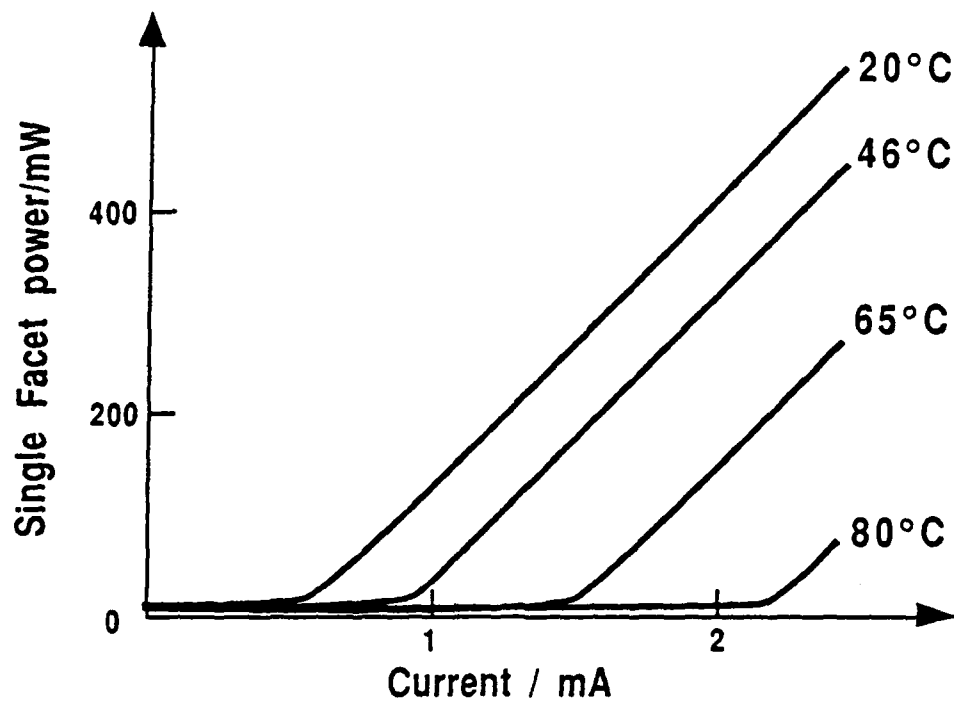


Figure 37 Light current characteristics for a broad area MQW laser from OF634

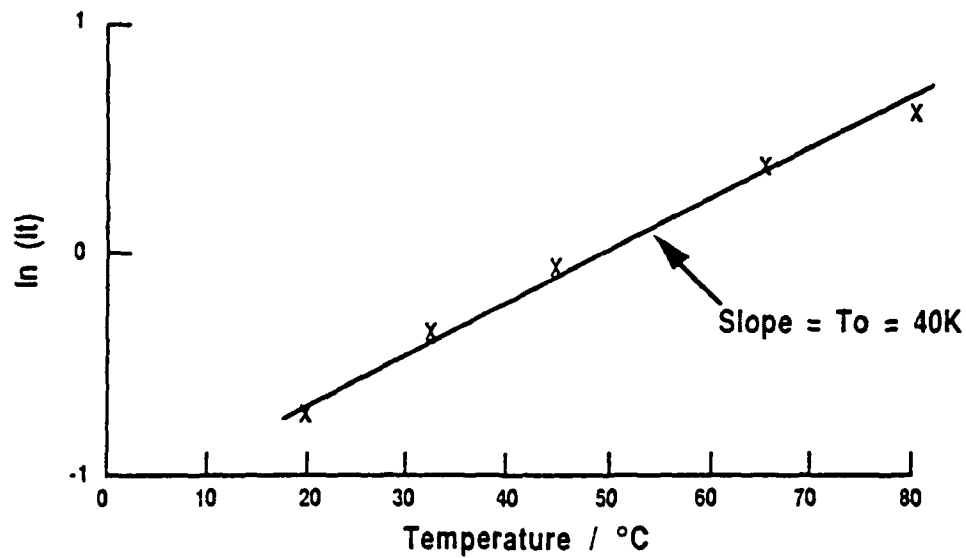


Figure 38 Plot of  $\log_e(\text{threshold current})$  as a function of temperature for a broad area laser from OF 634

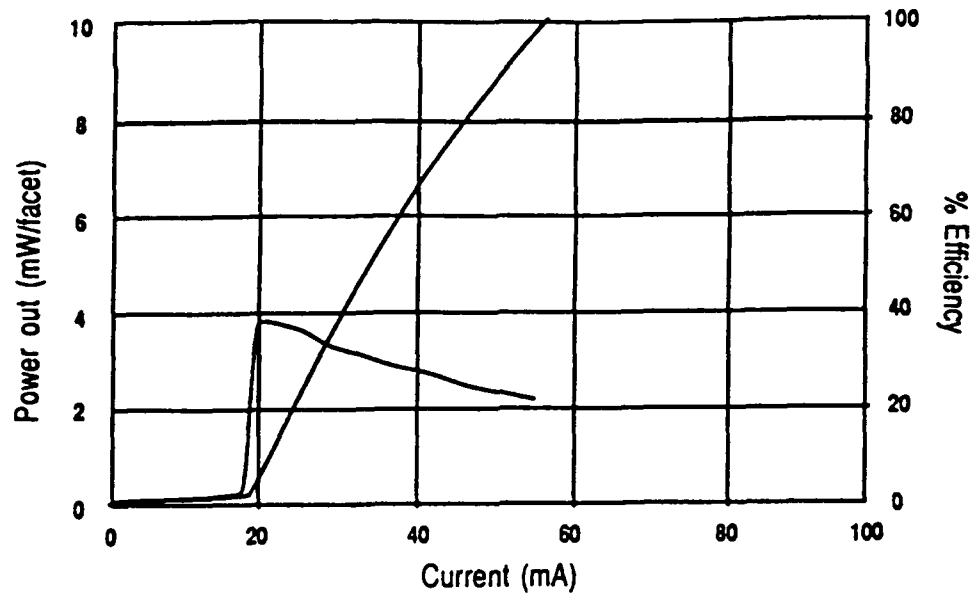


Figure 39 Light current characteristics for a buried ridge MQW laser from OF634

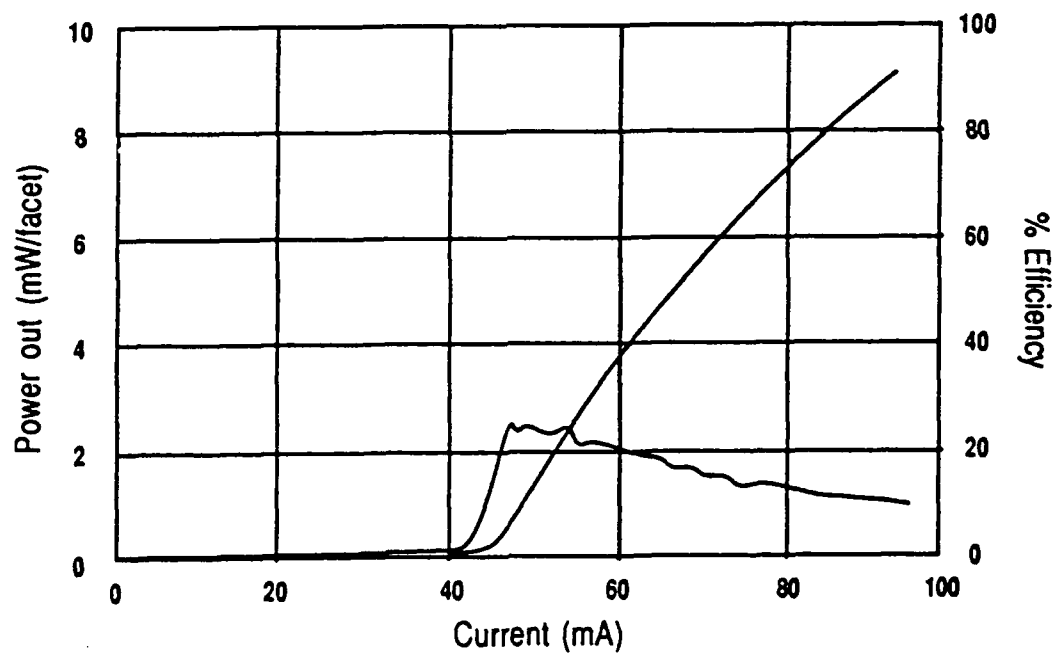


Figure 40 Light current characteristics for a buried ridge MQW laser from OF634 operating at 60°C

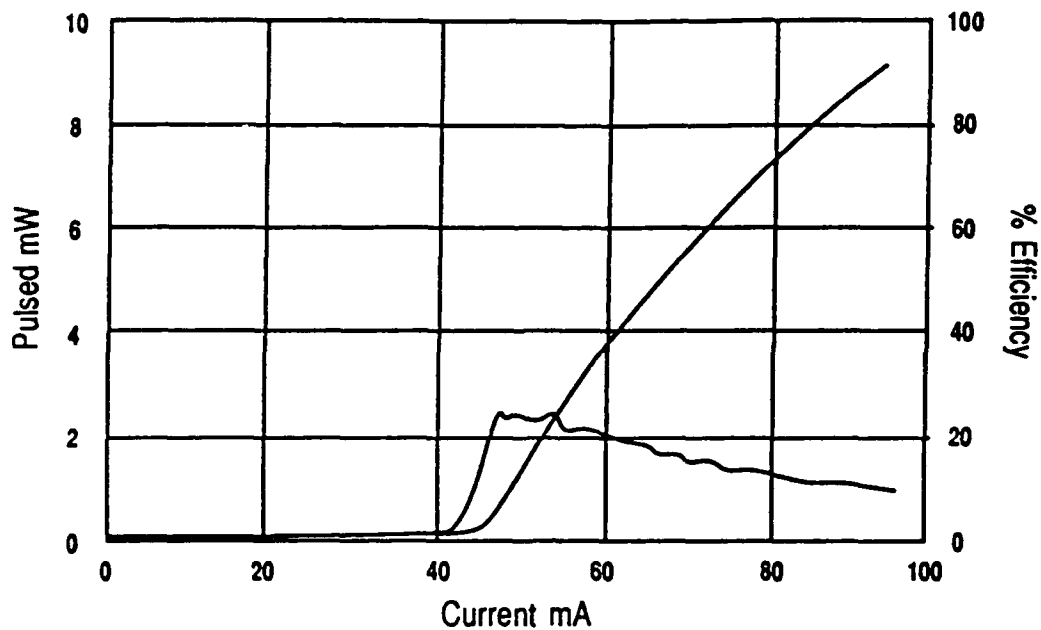


Figure 41 Light-current and efficiency plots for a high speed buried ridge laser from OF910

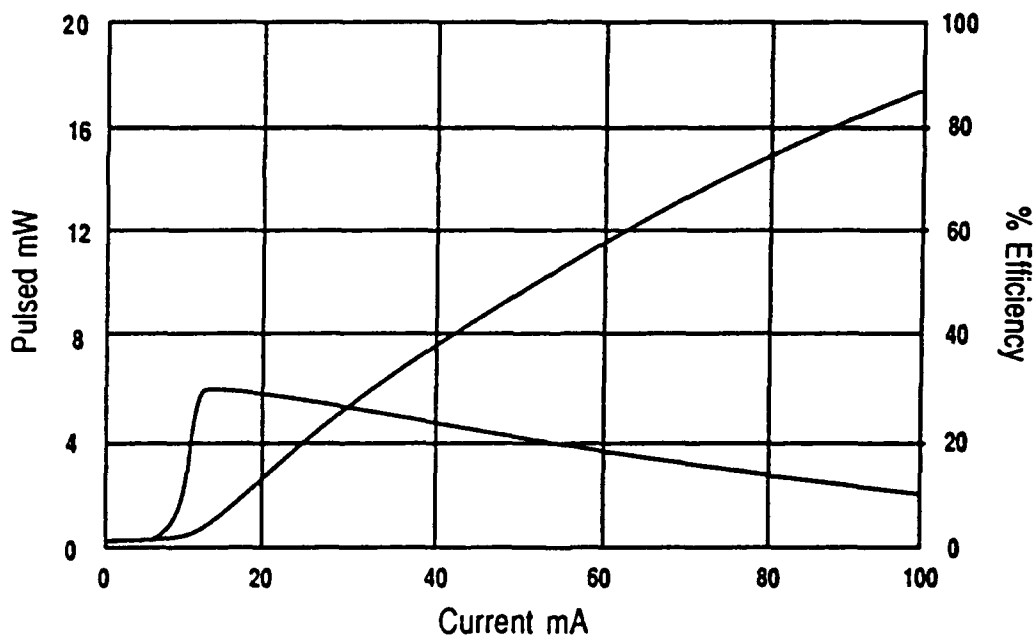


Figure 42 Light-current and efficiency plots for a high speed buried ridge laser from OF912

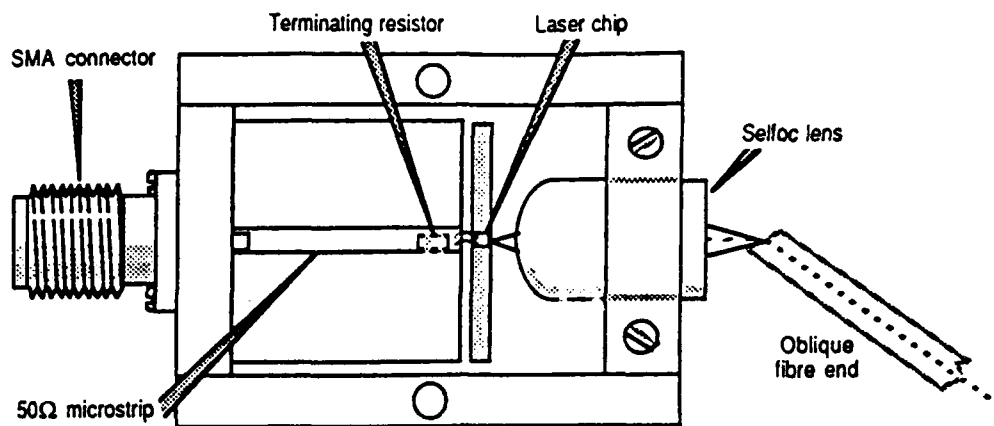


Figure 43 Schematic of high speed test fixture

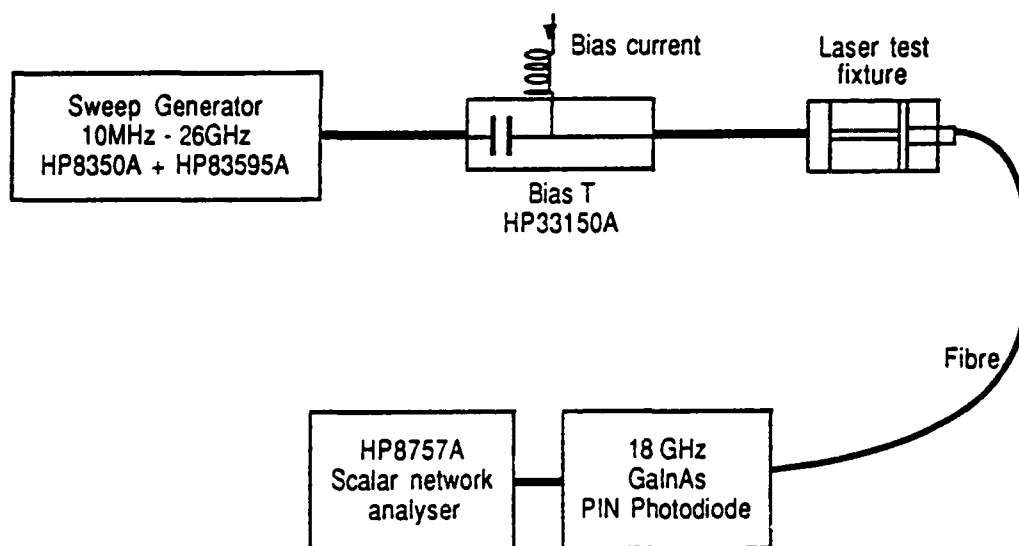


Figure 44 Schematic of high speed measurement system

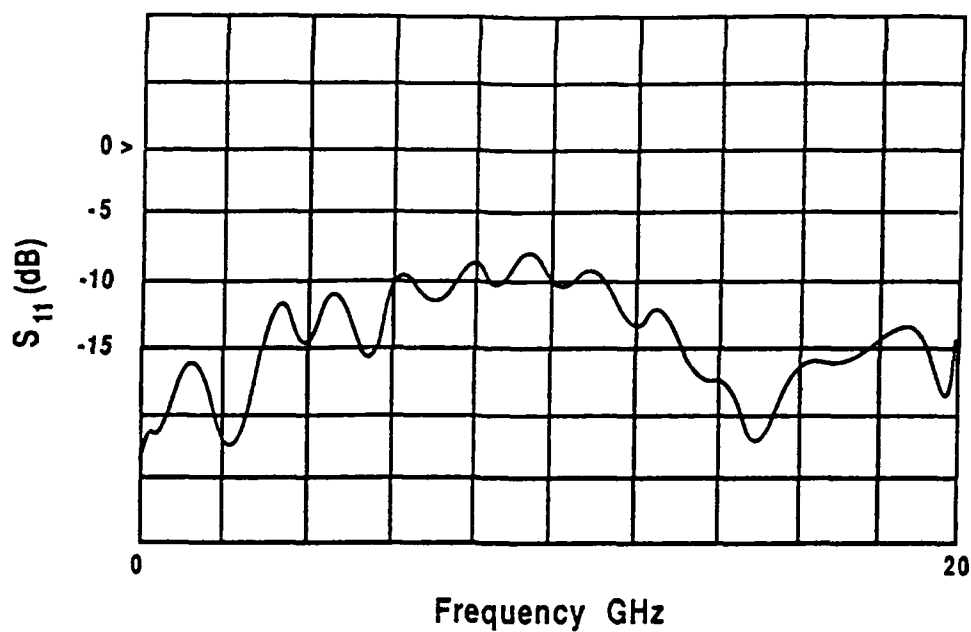


Figure 45 Plot of the  $S_{11}$  reflection parameter for the test jig up to 20GHz

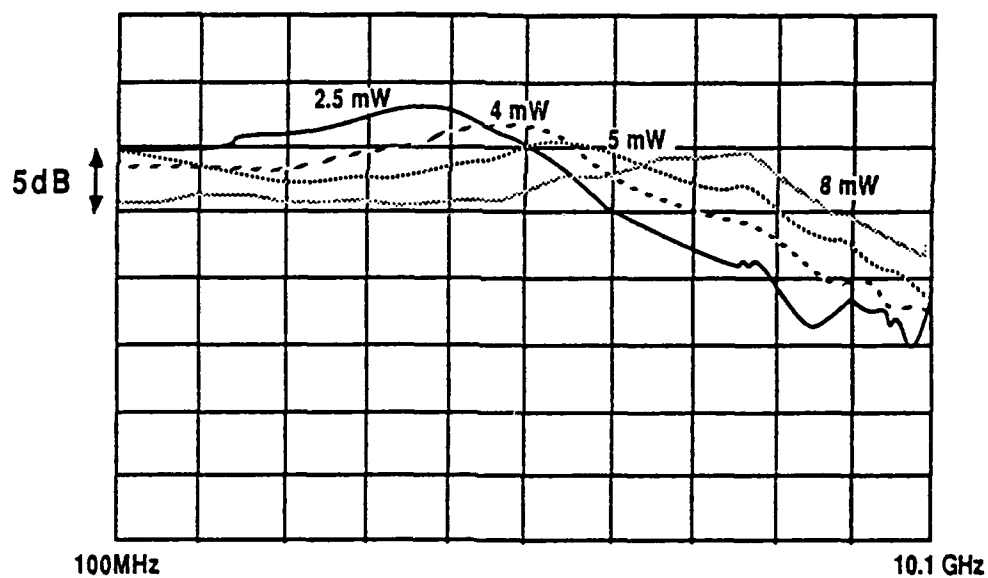


Figure 46 Small signal frequency response of chip OF912/33 (150 $\mu$ m long)

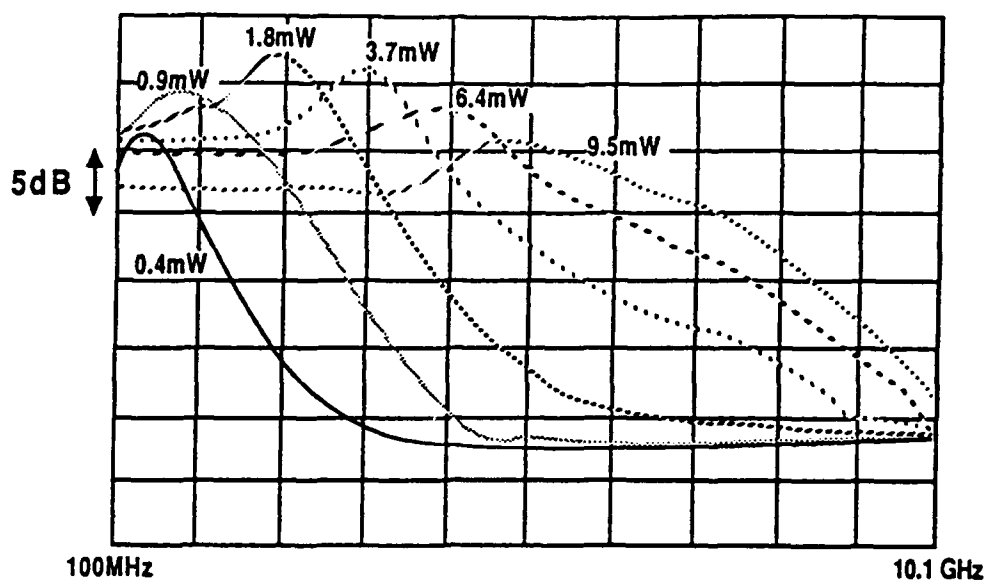


Figure 47 Small signal frequency response of chip OF912/62 (250μm long)

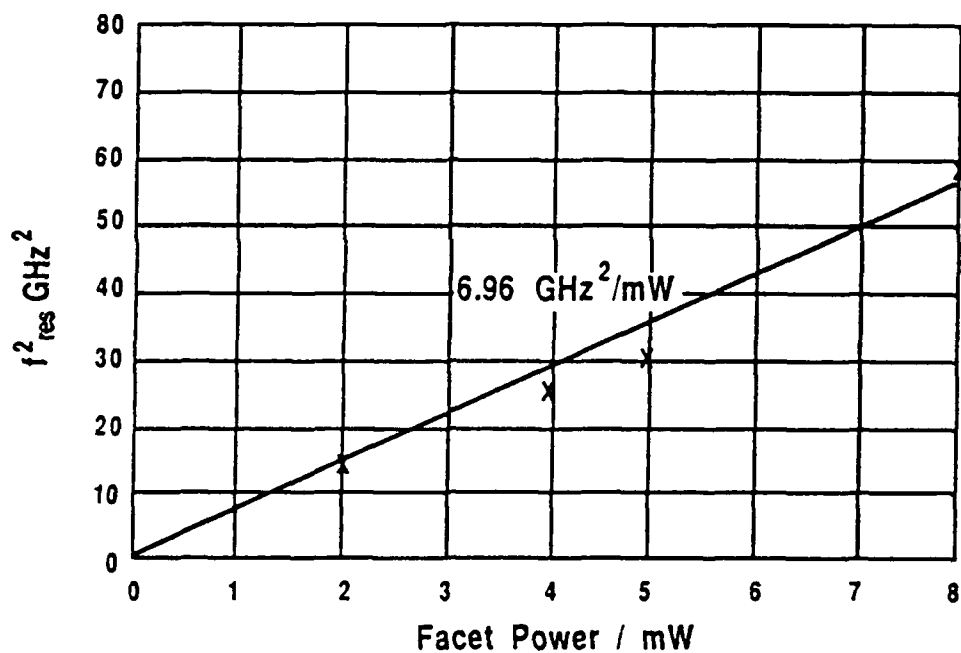


Figure 48 Plot of  $f_{res}^2$  as a function of facet output power for OF912/33



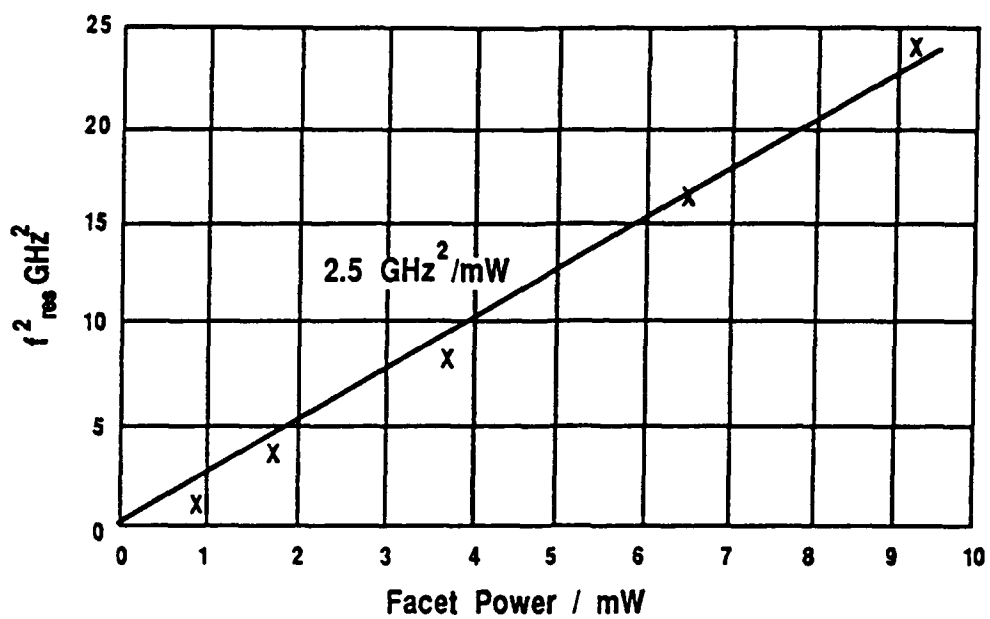


Figure 49 Plot of  $f_{res}^2$  as a function of facet output power for OF912/62

**MISSION  
OF  
ROME LABORATORY**

*Rome Laboratory plans and executes an interdisciplinary program in research, development, test, and technology transition in support of Air Force Command, Control, Communications and Intelligence (C<sup>3</sup>I) activities for all Air Force platforms. It also executes selected acquisition programs in several areas of expertise. Technical and engineering support within areas of competence is provided to ESD Program Offices (POs) and other ESD elements to perform effective acquisition of C<sup>3</sup>I systems. In addition, Rome Laboratory's technology supports other AFSC Product Divisions, the Air Force user community, and other DOD and non-DOD agencies. Rome Laboratory maintains technical competence and research programs in areas including, but not limited to, communications, command and control, battle management, intelligence information processing, computational sciences and software producibility, wide area surveillance/sensors, signal processing, solid state sciences, photonics, electromagnetic technology, superconductivity, and electronic reliability/maintainability and testability.*